Available online www.jsaer.com

***Journal of Scientific and Engineering Research*, 2017, 4(12):236-267**

Research Article

ISSN: 2394-2630
CODEN(USA): JSERBR

Spectral Method Applied to Entry Flows in Mars in 2D – High Order Analysis

Edisson Sávio de Góes Maciel

Instituto Tecnológico de Aeronáutica (ITA) – Rua Santa Clara, 245 – Cx. Postal: 2029, 12.243-970 – São José dos Campos – SP – Brazil

Abstract In the present work, a study involving a spectral method to solve the reactive Euler and Navier-Stokes equations under condition of entry flow in Mars is performed. The Euler and Navier-Stokes equations, in conservative and finite volume contexts, employing structured spatial discretization, are studied. The Van Leer and the Liou and Steffen Jr. schemes are used to perform the numerical experiments. The Euler backward method is applied to march the schemes in time. The spectral method presented in this work employs collocation points and variants of Chebyshev and Legendre interpolation functions are analyzed. The "hot gas" hypersonic flows around a blunt body and around a double ellipse in two-dimensions are simulated. The convergence process is accelerated to steady state condition through a spatially variable time step procedure, which has proved effective gains in terms of computational acceleration (see Maciel). The reactive simulations involve Mars atmosphere chemical model of nine species and fifty-three reactions, based on the Kay and Netter field model. N, O, N_2, O_2, NO, CO_2, C, CO, CN species are used to perform the numerical comparisons. The results have indicated that all Legendre variants of the spectral method predicted the stagnation temperature value with errors inferior to 25.00% for the inviscid case, whereas the Chebyshev variants of the spectral method predicted the stagnation temperature value with errors inferior to 13.00% for the viscous case.

Keywords Hypersonic flow; thermochemical non-equilibrium entry flows; Euler and Navier-Stokes equations; Mars entry; high order accuracy; spectral method

1. Introduction

There are several approaches for computationally modeling fluid dynamics. These include finite difference, finite element, and spectral methods to name a few. Finite element and finite difference methods are frequently used and offer a wide range of well-known numerical schemes. These schemes can vary in terms of computational accuracy but are typically of lower order of accuracy. If a more accurate solution is desired, it is common practice to refine the mesh either globally or in a region of interest. This can often be a complicated or time consuming process as global mesh refinement will greatly increase the computation time while local refinement requires an elaborated refinement operation [1].

Alternatively, polynomial refinement has been used to improve the solution accuracy and has been shown to converge more quickly than mesh refinement in some cases [2-3]. For finite difference methods, polynomial refinement is performed by including neighboring node values in a higher order polynomial [4]. This can increase the complexity of the scheme especially near the boundaries where nodes do not exist to construct the higher order polynomials. Finite element methods instead increase the number of unknown values within the cell itself to construct a higher order solution [5].

A scheme with a very high formal order of accuracy will not necessarily always produce the highest resolution. [6] demonstrated that a spectral-like scheme with a formal fourth-order accuracy produced a much more highly resolved solution than schemes with higher formal orders of accuracy when comparing modified wave numbers.

Therefore, formal order of accuracy does not provide a comprehensive basis for selecting the best solution procedure. State-of-art methods such as spectral methods fall into this category.

Spectral methods are considered a class of solution techniques using sets of known functions to solve differential equations [7]. Such methods are generally considered high order and capable of obtaining solutions with a high resolution. Unlike finite-difference and finite-element methods, spectral methods utilize an expansion in terms of global, rather than local, basis functions to represent the solution of a differential equation. When properly applied, these techniques accurately resolve phenomena on the scale of the mesh spacing. The order of truncation error decay with mesh refinement is also higher than which can be achieved with finite-difference and finite-element methods. For problems with smooth solutions, it is possible to produce spectral method whose truncation error goes to zero as faster than any finite power of the mesh spacing (exponential convergence).

Spectral methods may be viewed as an extreme development of the class of discretization schemes known by the generic name of method of weighted residuals (MWR) [8]. The key elements of the MWR are the trial functions (also called the expansion or approximating functions) and the test functions (also known as weighted functions). The trial functions are used as the basis functions for a truncated series expansion of the solution that, when substituted into the differential equation, produces the residual. The test functions are used to enforce the minimization of the residual.

The choice of the trial functions is what distinguishes the spectral methods from the element and finite difference methods. The trial functions for spectral methods are infinitely differentiable global functions (Typically, they are tensor products of the eigenfunctions of singular Sturm-Liouville problems). In the case of finite element methods, the domain is divided into small elements and a trial function is specified in each element. The trial functions are thus local in character and well suited for handling complex geometries. The finite difference trial functions are likewise local.

The choice of test function distinguishes between Galerkin and collocation approaches. In the Galerkin approach, the test functions are the same as the trial functions, whereas in the collocation approach the test functions are translated Dirac delta functions. In other words, the Galerkin approach is equivalent to a least-square approximation, whereas the collocation approach requires the differential equations to be solved exactly at the collocation points.

The collocation approach is the simplest of the MWR and appears to have been first used by [9] in his study of electronic energy bands in metals. A few years later, [10] applied this method to the problem of torsion in square prism. [11] developed it as a general method for solving ordinary differential equations. They used a variety of trials functions and an arbitrary distribution of collocation points. The work of [12] established for the first time that a proper choice of the trial functions and the distribution of collocation points are crucial to the accuracy of the solution. Perhaps he should be credited with laying down the foundation of the orthogonal collocation method.

Spectral methods have been used on one-dimensional, compressible flow problems with piecewise linear solutions by [13-14]. These reports demonstrated that spectral methods, when combined with appropriate filtering techniques, can capture one-dimensional shock waves in otherwise featureless flows. A different sort of demonstration was provided by [15]. They exhibited spectral solutions of compressible flows with nontrivial structures in the smooth regions.

There has been significant interest in recent years in a mission to Mars. One such proposal is the MARSNET assessment study [16] concerning the potential contribution of ESA (European Space Agency) to a Mars Network mission in cooperation with NASA. NASA is currently studying a network mission MESUR (Mars Environmental Survey), involving the placement of up twenty small scientific stations on the surface of Mars. The objective of the proposed ESA activities is the provision of three of these stations to perform a variety of scientific experiments. The intended entry scenario is an unguided ballistic entry at a typical velocity of 6 km/s using a blunt sphere/cone configuration in which deceleration is provided predominantly by hypersonic aero-braking. It is important that the mass of the vehicle structure and thermal protection system (TPS) be minimized such that the payload delivered to the surface may be maximized.

The trajectory for a ballistic Martian entry takes the vehicle through regions where thermochemical non-equilibrium effects in the surrounding shock layer may be significant. For typical entry velocities (> 5 km/s) the temperature in the shock layer will be sufficiently high for dissociation of the free stream species to occur. The energy removed through such reactions may be released at the vehicle surface via recombination leading to significantly enhanced heat transfer rates. In order to design the TPS for minimum mass the heat transfer rate needs to be accurately predicted. This requires that any catalytic properties of the TPS material are accounted for in the heat transfer rate calculation since these will determine the extent of wall recombination.

As aforementioned, missions to other planets remain an objective for the ESA, and such missions generally involve the entry of a space vehicle into the atmospheres of those planets. In the context of such entry, aerothermodynamics is one of the critical technologies. While the thermochemical behavior of air under re-entry conditions has been studied extensively, and is to some degree understood, the same is not true for entries into other atmospheres. The atmospheres of Mars and Venus, for example, contain significant amounts of carbon dioxide. In particular, the Mars atmosphere is a mixture of approximately 96% CO_2 and 4% N_2, with pressures much lower than the Earth's atmosphere, so for any entry into the Martian atmosphere the non-equilibrium behavior of CO_2 is likely to be of importance for a typical blunt body entry vehicle. This includes not just the influence of thermochemistry on the fore-body heat-shield flowfield, but also the influence on the shoulder expansion, base flow, and base heating environment.

In the present work, a study involving a spectral method to solve the reactive Euler and Navier-Stokes equations under condition of entry flow in Mars is performed. The Euler and Navier-Stokes equations, in conservative and finite volume contexts, employing structured spatial discretization, are studied. The [17-18] schemes are used to perform the numerical experiments. The Euler backward integration method is applied to march the schemes in time. The spectral method presented in this work employs collocation points and variants of Chebyshev and Legendre interpolation functions are analyzed. The "hot gas" hypersonic flows around a blunt body, and around a double ellipse in two-dimensions, are simulated. The convergence process is accelerated to steady state condition through a spatially variable time step procedure, which has proved effective gains in terms of computational acceleration [19-20]. The reactive simulations involve Mars atmosphere chemical model of nine species and fifty-three reactions, based on the [21] model. N, O, N_2, O_2, NO, CO_2, C, CO, CN species are used to perform the numerical comparisons. The results have indicated that all Legendre variants of the spectral method predicted the stagnation temperature value with errors inferior to 25.00% for the inviscid case, whereas the Chebyshev variants of the spectral method predicted the stagnation temperature value with errors inferior to 13.00% for the viscous case.

2. Spectral Method

Two classes of techniques for spectral discretization are referred to as tau and collocation methods [22]. The latter technique is used here. In this scheme, the approximation series is determined by satisfying the differential equation exactly at a set of distinct collocation points. The locations of these points in the domain are linked to the choice of basis function. In this study, arbitrary collocation points are implemented. The collocation method is used here since enforcement of boundary conditions and evaluations of nonlinear terms are straightforward. Additionally, some accuracy advantage is seen in the collocation method over the tau method for a number of problems [22]. The series expansion for a function Q(x) may be represented as

$$Q_N(x) = \sum_{n=0}^{N} \hat{Q}_n B_n(x), \quad (1)$$

where $B_n(x)$ are the basis functions and N is the total number of nodes employed in the interpolation process (it is also the order of accuracy of the spectral method). The coefficients $\hat{Q}_n$ are often termed the spectrum of $Q_N(x)$. One common technique used to evaluate the spectrum is to consider Eq. (1) as an interpolation series representing Q(x). The interpolation "nodes" of such series are the collocation points of the method. For a scheme based on Chebyshev collocation, the basis functions are:

$$B_n(x) = T_n(x) = 2xP_{n-1}(x) - P_{n-2}(x), n \geq 2, \quad (2)$$

with: $P_0(x) = 1$ and $P_1(x) = x$. The Chebyshev-Gauss-Lobatto standard collocation points are

$$x_l = \cos\left(\frac{\pi l}{N}\right), \qquad l = 0, 1, \ldots, N. \tag{3}$$

The Chebyshev collocation points result from a simple change of variables, which relates the Chebyshev interpolation series to a Fourier cosine series [22]. To evaluate the $\hat{Q}_n$, the inverse relation is required. This is

$$\hat{Q}_n = \hat{c}_n \sum_{l=0}^{N} w_l B_n(x_l) Q_{i,j}, \qquad n = 0, 1, \ldots, N, \tag{4}$$

With w_l being a normalized weighting function and $\hat{c}_n$ a constant. These variables assume the following expressions to a Chebyshev interpolation:

$$\hat{c}_n = \frac{2}{N\bar{c}_n}, \text{ where: } \bar{c}_n = \begin{cases} 2, & n = 0 \text{ or } N \\ 1, & 1 < n < N-1 \end{cases}; \text{ and } w_l = \frac{1}{\bar{c}_l}. \tag{5}$$

Legendre collocation is based on using Legendre polynomials as the basis function in Eq. (1), e.g.,

$$B_n(x) = \left[(2n-1)xP_{n-1}(x) - (n-1)P_{n-2}(x)\right]/n, \qquad n \geq 2, \tag{6}$$

where: $P_0(x) = 1$ and $P_1(x) = x$. Interpolation via Legendre series cannot easily be related to trigonometric interpolation, so there is no simple expression to evaluate the $\hat{Q}_n$ coefficients. Appeal must be made to the theory of numerical quadrature to form an approximation to the integrals which result from analytic Legendre interpolation [23]. Considering Eq. (4), the normalized weights and constant of the Legendre-Gauss-Lobatto collocation points are

$$w_l = \frac{1}{N(N+1)B_N^2(x_l)} \text{ and } \hat{c}_n = \begin{cases} 2n+1, & n = 0,1,\ldots,N-1 \\ N, & n = N \end{cases}. \tag{7}$$

In this work, it was assumed that the Legendre-Gauss-Lobatto collocation points are the same as the Chebyshev-Gauss-Lobatto ones. It was also adopted the following collocation points and normalized weights for the Chebyshev-Gauss-Radau interpolation, based on the work of [24]:

$$x_l = \cos\left(\frac{2\pi l}{2N+1}\right), \tag{8}$$

$$w_l = \begin{cases} \dfrac{N}{2N+1}, & l = 0 \\ \dfrac{N}{N+1}, & \text{elsewhere} \end{cases}. \tag{9}$$

For the Legendre-Gauss-Radau interpolation, also based in [24], the collocation points are defined by Eq. (8) and the normalized weights are described by:

$$w_l = \begin{cases} \dfrac{1}{(N+1)^2}, & l = 0 \\ \dfrac{1}{2(N+1)^2} \times \dfrac{1-x_l}{B_N(x_l)}, & \text{elsewhere} \end{cases} \tag{10}$$

The same calculation to the vector of conserved variables Q is applied to the vector of flux C, to be defined in section 4.

Hence, we have two collocation point options and two normalized weight functions to be considered by the Chebyshev and the Legendre methods, namely: Chebyshev-Gauss-Radau, Chebyshev-Gauss-Lobatto, Legendre-Gauss-Radau and Legendre-Gauss-Lobatto.

3. Reactive Euler and Navier-Stokes Equations in 2D

As the Euler equations are obtained from the Navier-Stokes equations when the Reynolds number tends to infinite, only the Navier-Stokes equations are presented. Hence, the flow is modeled by the Navier-Stokes equations and the condition of thermochemical non-equilibrium, where the rotational and vibrational

contributions are considered, is taken into account. For details of the chemical model adopted for the simulations, as well the thermodynamic and transport property calculations, the reader is encouraged to read [25-26]. The reactive Navier-Stokes equations in thermochemical non-equilibrium were implemented on conservative and finite volume contexts, in two-dimensions. In this case, these equations in integral and conservative forms are given by:

$$\frac{\partial}{\partial t}\int_V Q dV + \int_S \vec{F} \bullet \vec{n} dS = \int_V S_{CV} dV \text{, with: } \vec{F} = (E_e - E_v)\vec{i} + (F_e - F_v)\vec{j}, \quad (11)$$

where: Q is the vector of conserved variables, V is the volume of a computational cell, $\vec{F}$ is the complete flux vector, $\vec{n}$ is the unity vector normal to the flux face, S is the flux area, S_{CV} is the chemical and vibrational source term, E_e and F_e are the convective flux vectors or the Euler flux vectors in the x and y directions, respectively, and E_v and F_v are the viscous flux vectors in the x and y directions, respectively. The $\vec{i}$ and $\vec{j}$ unity vectors define the Cartesian coordinate system. Thirteen (13) conservation equations are solved: one of general mass conservation, two of linear momentum conservation, one of total energy, eight of species mass conservation, and one of the vibrational internal energy of the molecules. Therefore, one of the species is absent of the iterative process. The CFD literature recommends that the species of biggest mass fraction of the gaseous mixture should be omitted, aiming to result in a minor numerical accumulation error. To the present study, in which is chosen a chemical model to the Mars atmosphere composed of nine (9) chemical species (N, O, N_2, O_2, NO, CO_2, C, CO, CN) to the [21] model,this species can be the CO_2 or the N_2. To this work, the$CO_2$was chosen. The vectors Q, E_e, F_e, E_v, F_v, and S_{CV} can be defined as follows:

$$Q = \begin{Bmatrix} \rho \\ \rho u \\ \rho v \\ e \\ \rho_1 \\ \rho_2 \\ \rho_3 \\ \rho_4 \\ \rho_5 \\ \rho_7 \\ \rho_8 \\ \rho_9 \\ \rho e_V \end{Bmatrix}, E_e = \begin{Bmatrix} \rho u \\ \rho u^2 + p \\ \rho uv \\ \rho Hu \\ \rho_1 u \\ \rho_2 u \\ \rho_3 u \\ \rho_4 u \\ \rho_5 u \\ \rho_7 u \\ \rho_8 u \\ \rho_9 u \\ \rho e_V u \end{Bmatrix}, F_e = \begin{Bmatrix} \rho v \\ \rho uv \\ \rho v^2 + p \\ \rho Hv \\ \rho_1 v \\ \rho_2 v \\ \rho_3 v \\ \rho_4 v \\ \rho_5 v \\ \rho_7 v \\ \rho_8 v \\ \rho_9 v \\ \rho e_V v \end{Bmatrix}, E_v = \begin{Bmatrix} 0 \\ \tau_{xx}/Re \\ \tau_{xy}/Re \\ (f_x - \phi_x)/Re \\ -\rho_1 v_{1x}/Re \\ -\rho_2 v_{2x}/Re \\ -\rho_3 v_{3x}/Re \\ -\rho_4 v_{4x}/Re \\ -\rho_5 v_{5x}/Re \\ -\rho_7 v_{7x}/Re \\ -\rho_8 v_{8x}/Re \\ -\rho_9 v_{9x}/Re \\ (q_{v,x} - \phi_{v,x})/Re \end{Bmatrix}, F_v = \begin{Bmatrix} 0 \\ \tau_{xy}/Re \\ \tau_{yy}/Re \\ (f_y - \phi_y)/Re \\ -\rho_1 v_{1y}/Re \\ -\rho_2 v_{2y}/Re \\ -\rho_3 v_{3y}/Re \\ -\rho_4 v_{4y}/Re \\ -\rho_5 v_{5y}/Re \\ -\rho_7 v_{7y}/Re \\ -\rho_8 v_{8y}/Re \\ -\rho_9 v_{9y}/Re \\ (q_{v,y} - \phi_{v,y})/Re \end{Bmatrix}, \quad (12)$$

in which: ρ is the mixture density; u and v are Cartesian components of the velocity vector in the x and y directions, respectively; p is the pressure term; H is the fluid total enthalpy;ρ_1, ρ_2, ρ_3,ρ_4,ρ_5, ρ_7, ρ_8, andρ_9 are densities of the N, O, N_2,O_2, NO, C, CO, and CN, respectively; e_V is the sum of the vibrational energy of the molecules; the τ's are the components of the viscous stress tensor; f_x and f_y are viscous work and Fourier heat flux functions; $\rho_s v_{sx}$ and $\rho_s v_{sy}$ represent the species diffusion flux, defined by the Fick law; ϕ_x and ϕ_y are the terms of mixture diffusion; $\phi_{v,x}$ and $\phi_{v,y}$ are the terms of molecular diffusion calculated at the vibrational temperature; $\dot{\omega}_s$ is the chemical source term of each species equation, defined by the law of mass action; e_v^* is the molecular-vibrational-internal energy calculated with the translational/rotational temperature; τ_s is the

translational-vibrational characteristic relaxation time of each molecule; $q_{v,x}$ and $q_{v,y}$ are the vibrational Fourier heat flux components in the x and y directions, respectively; Re is the laminar Reynolds number.

$$S_{CV} = \left\{ 0 \quad 0 \quad 0 \quad 0 \quad \dot{\omega}_1 \quad \dot{\omega}_2 \quad \dot{\omega}_3 \quad \dot{\omega}_4 \quad \dot{\omega}_5 \quad \dot{\omega}_7 \quad \dot{\omega}_8 \quad \dot{\omega}_9 \quad \sum_{s=mol} \rho_s \left(e^*_{v,s} - e_{v,s} \right) / \tau_s + \sum_{s=mol} \dot{\omega}_s e_{v,s} \right\}^T . \quad (13)$$

The viscous stresses, in N/m^2, are determined, according to a Newtonian fluid model, by:

$$\tau_{xx} = \left[2\mu_m \, \partial u/\partial x - 2/3 \mu_m \left(\partial u/\partial x + \partial v/\partial y \right) \right] ;$$
$$\tau_{xy} = \mu_m \left(\partial u/\partial y + \partial v/\partial x \right); \quad (14)$$
$$\tau_{yy} = \left[2\mu_m \left(\partial v/\partial y \right) - 2/3 \mu_m \left(\partial u/\partial x + \partial v/\partial y \right) \right],$$

where μ_m is the molecular viscosity. Expressions to f_x and f_y are given below:

$$f_x = \tau_{xx} u + \tau_{xy} v + q_x + q_{v,x} ; \quad (15)$$

$$f_y = \tau_{xy} u + \tau_{yy} v + q_y + q_{v,y} , \quad (16)$$

Where q_x and q_y are the Fourier heat flux components and are given by:

$$q_x = k_{TR} \, \partial T/\partial x ; \quad (17)$$

$$q_y = k_{TR} \, \partial T/\partial y , \quad (18)$$

Where k_{TR} is the thermal conductivity due to translation and rotational modes. The $q_{v,x}$ and $q_{v,y}$ are the vibrational heat flux components and are given by:

$$q_{v,x} = k_V \, \partial T_V / \partial x ; \quad (19)$$

$$q_{v,y} = k_V \, \partial T_V / \partial y , \quad (20)$$

with k_V being the vibrational thermal conductivity and T_V is the vibrational temperature, what characterizes this model as of two temperatures: translational/rotational and vibrational. The terms of species diffusion, defined by the Fick law, to a condition of thermal non-equilibrium, are determined by ([27]):

$$\rho_s v_{sx} = -\rho D_s \frac{\partial Y_{MF,s}}{\partial x} \text{ and } \rho_s v_{sy} = -\rho D_s \frac{\partial Y_{MF,s}}{\partial y} , \quad (21)$$

with "s" referent to a given species, $Y_{MF,s}$ being the molar fraction of the species, defined as:

$$Y_{MF,s} = \frac{\rho_s / M_s}{\sum_{k=1}^{ns} \rho_k / M_k} \quad (22)$$

and D_s is the species-effective-diffusion coefficient. "ns" is the total number of species of the chemical model. The Reynolds number is defined as

$$Re = \rho_{char} V_{initial} L / \mu_{char} , \quad (23)$$

Where "char" represents characteristic or freestream properties, $V_{initial}$ represents the flow initial velocity, μ_{char} is the characteristic molecular viscosity, and L is a characteristic length of the studied configuration. The diffusion terms ϕ_x and ϕ_y which appear in the energy equation are defined by ([28]):

$$\phi_x = \sum_{s=1}^{ns} \rho_s v_{sx} h_s \text{ and } \phi_y = \sum_{s=1}^{ns} \rho_s v_{sy} h_s , \quad (24)$$

Being h_s the specific enthalpy (sensible) of the chemical species "s". The molecular diffusion terms calculated at the vibrational temperature, $\phi_{v,x}$ and $\phi_{v,y}$, which appear in the vibrational-internal-energy equation are defined by [27]:

$$\phi_{v,x} = \sum_{s=mol} \rho_s v_{sx} h_{v,s} \text{ and } \phi_{v,y} = \sum_{s=mol} \rho_s v_{sy} h_{v,s} , \quad (25)$$

With $h_{v,s}$ being the specific enthalpy (sensible) of the chemical species "s" calculated at the vibrational temperature T_V. The sum of Eq. (13), as also those present in Eq. (25), considers only the molecules of the system, namely: N_2, O_2, NO, CO_2, CO, and CN.

4. Numerical Algorithms

Considering the two-dimensional and structured case, the flux vector splitting algorithms follow that described in [25-26, 29-30]. The system is solved in three parts separately, according to [31]. The first part takes into account the dynamic part, which considers the Navier-Stokes equations, the second one takes into account the chemical part involving the chemical contributions, and finally, the third part considers only the vibrational contribution. Hence, the discrete-dynamic-convective flux, which solves the dynamic part, is given by:

$$R_{i+1/2,j} = |S|_{i+1/2,j}\left\{\frac{1}{2}M_{i+1/2,j}\left[\begin{pmatrix}\rho a\\ \rho a u\\ \rho a v\\ \rho a H\end{pmatrix}_L + \begin{pmatrix}\rho a\\ \rho a u\\ \rho a v\\ \rho a H\end{pmatrix}_R\right] - \frac{1}{2}\phi_{i+1/2,j}\left[\begin{pmatrix}\rho a\\ \rho a u\\ \rho a v\\ \rho a H\end{pmatrix}_R - \begin{pmatrix}\rho a\\ \rho a u\\ \rho a v\\ \rho a H\end{pmatrix}_L\right]\right\} + \begin{pmatrix}0\\ S_x p\\ S_y p\\ 0\end{pmatrix}_{i+1/2,j} \quad (26)$$

with $S_{i+1/2,j} = \begin{bmatrix}S_x & S_y\end{bmatrix}^t_{i+1/2,j}$ defining the normal area vector for the surface (i+½,j). The normal area components S_x and S_y to each flux interface are given in Tab. 1. The discrete-chemical-convective flux is defined by:

$$R_{i+1/2,j} = |S|_{i+1/2,j}\left\{\frac{1}{2}M_{i+1/2,j}\left[\begin{pmatrix}\rho_1 a\\ \rho_2 a\\ \rho_3 a\\ \rho_4 a\\ \rho_5 a\\ \rho_7 a\\ \rho_8 a\\ \rho_9 a\end{pmatrix}_L + \begin{pmatrix}\rho_1 a\\ \rho_2 a\\ \rho_3 a\\ \rho_4 a\\ \rho_5 a\\ \rho_7 a\\ \rho_8 a\\ \rho_9 a\end{pmatrix}_R\right] - \frac{1}{2}\phi_{i+1/2,j}\left[\begin{pmatrix}\rho_1 a\\ \rho_2 a\\ \rho_3 a\\ \rho_4 a\\ \rho_5 a\\ \rho_7 a\\ \rho_8 a\\ \rho_9 a\end{pmatrix}_R - \begin{pmatrix}\rho_1 a\\ \rho_2 a\\ \rho_3 a\\ \rho_4 a\\ \rho_5 a\\ \rho_7 a\\ \rho_8 a\\ \rho_9 a\end{pmatrix}_L\right]\right\}, \quad (27)$$

and finally the discrete-vibrational-convective flux is defined as:

$$R_{i+1/2,j} = |S|_{i+1/2,j}\left\{\frac{1}{2}M_{i+1/2,j}\left[(\rho e_v a)_L + (\rho e_v a)_R\right] - \frac{1}{2}\phi_{i+1/2,j}\left[(\rho e_v a)_R - (\rho e_v a)_L\right]\right\}, \quad (28)$$

where "a" is the speed of sound, defined in section 5. For better comprehension, Fig. 1 exhibits the computational cell adopted for the simulations, as well its respective nodes and flux interfaces. C can be defined as the sum of the fluxes in each interface.

The same definitions presented in [25-26, 29-30] are valid to these algorithms. The definition of the dissipation term ϕ determines the particular formulation of the convective fluxes. The choice below corresponds to the [17] scheme, according to [32]:

$$\phi_{i+1/2,j} = \phi^{VL}_{i+1/2,j} = \begin{cases}|M_{i+1/2,j}|, & \text{if } |M_{i+1/2,j}| \geq 1;\\ |M_{i+1/2,j}| + 0.5(M_R - 1)^2, & \text{if } 0 \leq M_{i+1/2,j} < 1;\\ |M_{i+1/2,j}| + 0.5(M_L + 1)^2, & \text{if } -1 < M_{i+1/2,j} \leq 0.\end{cases} \quad (29)$$

and the [18] scheme is obtained by, according to [32]:

$$\phi_{i+1/2,j} = \phi^{LS}_{i+1/2,j} = |M_{i+1/2,j}|. \quad (30)$$

Both schemes are first-order accurate in space and in time. The high-order spatial accuracy is obtained, in the current study, by the spectral method.

The viscous formulation follows that of [33], which adopts the Green theorem to calculate primitive variable gradients. The viscous gradients at the interface are obtained by arithmetical average between cell (i,j) and its neighbors. As was done with the convective terms, there is a need to separate the viscous flux in three parts: dynamic viscous flux, chemical viscous flux, and vibrational viscous flux. The dynamic part corresponds to the first four equations of the Navier-Stokes ones, the chemical part corresponds to the eight equations immediately below the energy equation, and the vibrational part corresponds to the equation that follows the last chemical one.

The Euler backward method is used to perform time integration. This method is first-order accurate in time, to the three types of complete flux. To the convective dynamic component, this method can be represented in general form by:

$$Q_{i,j}^{(n+1)} = Q_{i,j}^{(n)} - \left(\Delta t_{i,j} / V_{i,j}\right) \times \left[C\left(Q_{i,j}^{(n)}\right)\right], \tag{31}$$

to the convective chemical component, it can be represented in general form by:

$$Q_{i,j}^{(n+1)} = Q_{i,j}^{(n)} - \Delta t_{i,j} \times \left\{C\left(Q_{i,j}^{(n)}\right) / V_{i,j} - S_C\left(Q_{i,j}^{(n)}\right)\right\}, \tag{32}$$

where the chemical source term S_C is calculated with the temperature T_{rrc} (reaction rate controlling temperature, see [25-26, 29-30]). Finally, to the convective vibrational component:

$$Q_{i,j}^{(n+1)} = Q_{i,j}^{(n)} - \Delta t_{i,j} \times \left\{C\left(Q_{i,j}^{(n)}\right) / V_{i,j} - S_V\left(Q_{i,j}^{(n)}\right)\right\}, \tag{33}$$

in which:

$$S_V = \sum_{s=mol} q_{T-V,s} + \sum_{s=mol} S_{C,s} e_{v,s}\,, \tag{34}$$

Where $q_{T\text{-}V}$ is the heat flux due to translational-vibrational relaxation, defined in Eq. (13) and in [25-26, 29-30].

5. Spatially Variable Time Step

The spatially variable time step has proved efficient gains in terms of convergence acceleration, as verified by [19-20]. Initially, the parameter σ is determined, where:

$$\sigma_s = \frac{c_s}{M_s} \text{ and } \sigma = \sum_{s=1}^{ns} \sigma_s\,, \tag{35}$$

With c_s being the mass fraction and M_s the molecular weight. The total specific heat at constant volume due to translation is defined as:

$$c_{V,T} = \sum_{s=1}^{ns} \sigma_s c_{V,T,s}\,, \tag{36}$$

where, for each gas constituent of the nine (9) species chemical model, the specific heat at constant volume, based on the kinetic theory of gases ([34]), is defined by

$$c_{V,T,N} = \frac{3}{2} R_N,\ c_{V,T,O} = \frac{3}{2} R_O,\ c_{V,T,N_2} = \frac{5}{2} R_{N_2},\ c_{V,T,O_2} = \frac{5}{2} R_{O_2},\ c_{V,T,NO} = \frac{5}{2} R_{NO}; \tag{37}$$

$$c_{V,T,CO_2} = \frac{5}{2} R_{CO_2},\ c_{V,T,C} = \frac{3}{2} R_C,\ c_{V,T,CO} = \frac{5}{2} R_{CO},\ c_{V,T,CN} = \frac{5}{2} R_{CN}, \tag{38}$$

Being R_s the specific gas constant. The total pressure of the gaseous mixture is determined by Dalton law, which indicates that the total pressure of the gas is the sum of the partial pressure of each constituent gas, resulting in:

$$p_s = c_s \rho R_s T \text{ and } p = \sum_{s=1}^{ns} p_s\,. \tag{39}$$

The speed of sound to a thermochemical non-equilibrium reactive mixture can be determined by

$$a = \sqrt{\frac{(1+\beta)p}{\rho}}, \tag{40}$$

where $\beta = \frac{R_{univ}\sigma}{c_{V,T}}$, with R_{univ} = 1.987 cal/(g-mol.K). Finally, the spatially variable time step is defined from the CFL (Courant-Friedrichs-Lewis) definition:

$$\Delta t_{i,j} = \frac{CFL\Delta s_{i,j}}{\sqrt{u_{i,j}^2 + v_{i,j}^2} + a_{i,j}}, \tag{41}$$

where $\Delta s_{i,j}$ is the characteristic length of each cell (defined between the minimum cell side length and the minimum centroid distance between each cell and its neighbors).

6. Dimensionless Scales, Initial and Boundary Conditions

6.1. Dimensionless Scales

The dimensionless scales employed to the reactive equations consisted in: R_s is dimensionless by a_{char}, wherea_{char} is calculated according to [25-26, 29-30]; c_v is dimensionless by a_{char}; h_s and Δh_s^0 are dimensionless by a_{char}^2; T and T_v, translational/rotational temperature and vibrational temperature, respectively, are dimensionless by a_{char}; ρ_s and ρ are dimensionless by ρ_{char}; u and v are dimensionless by a_{char}; μ is dimensionless by μ_{char}; D, diffusion coefficient, dimensionless by $a_{char}^2\, dt_{char}$, where dt_{char} is the minimum time step calculated in the computational domain at the first iteration; $\dot{\omega}$ is dimensionless by $(\rho_{char}/dt_{char})x10^{-3}$; e_v is dimensionless by a_{char}^2; p and e are dimensionless by $\rho_{char}a_{char}^2$; and τ_s, relaxation time, is dimensionless by dt_{char}. The characteristic properties are defined in [35].

6.2. Initial Condition

The initial conditions to both problems, for anine species chemical model are presented in Tabs. 2 and 3. The Reynolds number is obtained from data of [35].

6.3. Boundary Conditions

The boundary conditions are basically of three types: solid wall, entrance, and exit. These conditions are implemented with the help of ghost cells.

Wall condition. In the inviscid case, this condition imposes the flow tangency at the solid wall. This condition is satisfied considering the wall tangent velocity component of the ghost volume as equals to the respective velocity component of its real neighbor cell. At the same way, the wall normal velocity component of the ghost cell is equaled in value, but with opposite signal, to the respective velocity component of the real neighbor cell. It results in:

$$n_x = \Delta y/\sqrt{\Delta x^2 + \Delta y^2}; \quad \text{and } n_y = -\Delta x/\sqrt{\Delta x^2 + \Delta y^2}; \tag{42}$$

where, for the (i+1/2,j) interface:

$$\Delta x = x_{i+1,j+1} - x_{i+1,j}; \quad \text{and} \quad \Delta y = y_{i+1,j+1} - y_{i+1,j}. \tag{43}$$

Hence, the ghost cell velocity components are written as:

$$u_g = (n_y^2 - n_x^2)u_r - (2n_x n_y)v_r; \quad \text{and} \quad v_g = -(2n_x n_y)u_r + (n_x^2 - n_y^2)v_r. \tag{44}$$

with "g" related with ghost cell and "r" related with real cell. To the viscous case, the boundary condition imposes that the ghost cell velocity components be equal to the real cell velocity components, with negative signal:

$$u_g = -u_r \text{ and } v_g = -v_r. \quad (45)$$

The normal pressure gradient of the fluid at the wall is assumed to be equal to zero according to a boundary-layer like condition in the viscous case. The same hypothesis is applied for the normal temperature gradient at the wall, assuming an adiabatic wall. From these considerations, density and translational/rotational temperature are extrapolated from the respective values of its real neighbor volume (zero order extrapolation). The total vibrational internal energy is also extrapolated.

With the mixture species mass fractions and with the values of the respective specific heats at constant volume, it is possible to obtain the mixture specific heat at constant volume. The mixture formation enthalpy is extrapolated from the real cell. The mixture total energy to the ghost cell is calculated by:

$$e_g = \rho\left[c_{v\,mixt,g} T_{tr,g} + \left(\Delta h^0_{mixt,g} - R_{mixt} T_{REF}\right) + e_{v,g} + 0.5\left(u_g^2 + v_g^2\right)\right], \quad (46)$$

Where details of the calculation of $c_{v,mixt,g}$, of R_{mixt}, and of the vibrational energy are found in [25-26, 29-30].To the species density, the non-catalytic condition is imposed, what corresponds to zero order extrapolation from the real cell.

Entrance condition

It is divided in two flow regimes:

(a) Subsonic flow: Three properties are specified and one extrapolated in the boundary conditions of the dynamic part of the algorithm. This approach is based on information propagation analysis along characteristic directions in the calculation domain [36]. In other words, for subsonic flow, three characteristics propagate information pointing into the computational domain. Thus three flow properties must be fixed at the inlet plane. Just one characteristic line allows information to travel upstream. So, one flow variable must be extrapolated from the interior grid to the inlet boundary. The total energy was the extrapolated variable from the real neighbor volumes, for the studied problems. Density and velocity components adopted values of the initial flow. To the chemical part, eight information propagate upstream because it is assumed that all eight equations are conducted by the eigenvalue "$(q_n$-a)". In the subsonic flow, all eigenvalues are negative and the information should be extrapolated. In the same reasoning to the chemical boundary conditions, the vibrational-internal-energy equation is dictated by the "$(q_n$-a)" eigenvalue and, in the subsonic region, its value is negative. Hence, the vibrational internal energy should be extrapolated.

(b) Supersonic flow: In this case no information travels upstream; therefore all variables are fixed with their initial values.

Exit condition

It is also divided in two flow regimes:

(a) Subsonic flow: Three characteristic propagates information outward the computational domain. Hence, the associated variable should be extrapolated from interior information. The characteristic direction associated to the "$(q_{normal}$-a)" velocity should be specified because it points inward to the computational domain [36]. In this case, the ghost volume total energy is specified from its initial value. Density and velocity components are extrapolated. To the chemical part, the eigenvalue "$(q_n$-a)" is again negative and the characteristics are always flowing into the computational domain. Hence, the eight chemical species under study should have their densities fixed by their initial values. In the same reasoning, the internal vibrational energy should have its value prescribed by its initial value due to the eigenvalue "$(q_n$-a)" be negative.

(b) Supersonic flow: All variables are extrapolated from interior grid cells, as no flow information can make its way upstream. In other words, nothing can be fixed.

7. Physical Problems

Two physical problems were solved in this work, namely: blunt body physical problem, and double ellipse physical problem. For the first problem the geometry under study is a blunt body with 0.85m of nose ratio and inclined rectilinear walls of 10^o. The far field is located at 20.0 times the nose ratio in relation to the configuration nose. A mesh composed of 3,776 rectangular cells and 3,900 nodes was studied for the inviscid

case. This mesh is equivalent in finite differences to a one of 65x60 points. To the viscous case, a mesh of 2,646 rectangular cells and 2,750 nodes, with an exponential stretching of 5.0%, was analyzed, which is equivalent in finite differences to 55x50 points. A "O" mesh was taken as the base to construct both meshes. No smoothing was used in this mesh generation process, being this one constructed in Cartesian coordinates. Figure 2 shows the blunt body geometry for this study. Figures 3 and 4 exhibit the inviscid and viscous meshes.

The double ellipse problem is the second under study. The mesh is composed of 4,116 rectangular cells and 4,250 nodes, with an exponential stretching of 5.0% for the viscous case, and far field located at 20.0 unities. This mesh is equivalent in finite differences to a one of 85x50 points. Figure 5 shows the double ellipse geometry and Figs. 6 and 7 exhibit the inviscid and viscous meshes.

8. Results

Tests were performed in a Core i7 processor of 2.4 GHz and 6.0 Gbytes of RAM microcomputer, in a Windows 7.0 environment. Three (3) orders of reduction of the maximum residual in the field were considered to obtain a converged solution. The residual was defined as the value of the discretized conservation equation. In the convective dynamic part, such definition results in:

$$\text{Residual} = -\left(\Delta t_{i,j}/V_{i,j}\right)\times C_{i,j}. \quad (47)$$

The attack angle was adopted equal to zero.For the blunt body and the double ellipse problems, a 5^{th} order spectral method was employed in the inviscid numerical simulations and a 8^{th} order spectral method was employed in the viscous numerical simulations. For a matter of simplification, the following abbreviations are employed: [17] scheme = VL, [18] scheme = LS, Chebyshev-Gauss-Radau = CGR, Chebyhsev-Gauss-Lobatto = CGL, Legendre-Gauss-Radau = LGR, and Legendre-Gauss-Lobatto = LGL.

8.1. Blunt Body Problem

Inviscid case

Figures 8 to 11 show the pressure and translational/rotational temperature contours obtained by the VL and LS schemes as using the CGR collocation points. As can be seen, the solutions present good symmetry properties, being the LS solution less dissipative than the VL solution. The peaks of pressure for both schemes differ by a value of almost 100.0 unities. The temperature peaks differ by a factor of approximately 100.0K. Good symmetry properties are also observed in the temperature contours.

Figures 12 to 15 exhibit the pressure and temperature contours generated by the VL and LS schemes as using the CGL collocation points. Comparing Figs. 12 and 13 for the pressure contours, it is evident the less dissipative effects of the LS scheme. The pressure peaks are very close. Figures 14 and 15 present the temperature contours obtained by both schemes. The VL solution presents a temperature peak approximately 300K colder than the LS solution. Good symmetry properties are observed in both figures.

Figures 16 to 19 show the pressure and temperature contours calculated by the VL and LS schemes when using the LGR collocation points. Good symmetry properties are observed. The pressure peaks differ approximately of 50.0 unities. The temperature contours present good homogeneous properties. The VL temperature peak is almost 1,000K hotter than the LS temperature peak.

Figures 20 to 23 exhibit the pressure and temperature contours obtained by the VL and LS schemes as using the LGL collocation points. The pressure peaks differ of approximately 70.0 unities, being the LS solution more severe. Figures 22 and 23 present the translational/rotational temperature contours. The VL temperature peak is approximately 1,200K hotter than the LS temperature peak. Good homogeneous properties are observed in both solutions.

Viscous case. Figures 24 to 27 show the pressure and temperature contours obtained by the VL and LS numerical algorithms as using the CGR collocation points. In terms of pressure contours, both solutions present different aspects. The normal shock wave calculated by the VL scheme is more developed and more spreading than the LS one. The pressure peaks differ by approximately 60.0 unities, being the VL peak more intense than the LS peak. The translational/rotational temperature contours generated by the VL scheme is hotter than the respective temperature contours generated by the LS scheme. The shock wave is more developed in the VL solution.

Figures 28 to 31 exhibit the pressure and temperature contours calculated by the VL and LS numerical schemes when using the CGL collocation points. The pressure contours are more developed in the VL solution, with the pressure peak approximately 40.0 unities more severe than the LS solution. Good symmetry properties are observed in both solutions. In the temperature contours, the VL temperature peak is almost 2,000K hotter than the LS temperature peak. Good homogeneous properties are observed in both figures.

Figures 32 to 35 show pressure and temperature contours obtained by the VL and LS numerical algorithms as using the LGR collocation points. Figures 32 and 33 present the pressure contours and the LS solution is more severe than the VL solution. In this case, the VL solution was less dissipative and more developed than the LS solution. Figure 34 and 35 exhibit the translational/rotational temperature contours obtained by both schemes. The VL's temperature contours are more intense than LS' temperature contours, the difference in terms of temperature peaks is quasi 2,200K in favor of the VL scheme. Good symmetry and homogenous properties are observed in both solutions.

Figure 36 to 39 exhibit the pressure and temperature contours calculated by the VL and LS schemes when using the LGL collocation points. The pressure peaks differ of approximately 20.0 unities in favor of the LS solution. The VL solution is less dissipative than the LS solution. Figures 38 and 39 show the temperature contours obtained by both schemes. The normal shock wave generated by the VL scheme is more intense and hotter than that generated by the LS scheme. The temperature peaks differ by approximately 2,200K, being hotter in VL solution. Good symmetry and homogeneous properties are observed in both solutions.

8.2. Double Ellipse Problem

Inviscid case.Figures 40 to 43 show the pressure and translational/rotational temperature contours obtained by the VL and LS schemes as using the CGR collocation points. The highest pressure peak is obtained by the LS solution, being about 10.0 unities more severe than the respective VL solution. Both schemes capture the two normal shock waves at the bigger and minor ellipses. Figures 42 and 43 exhibit the temperature contours, where the LS scheme detects the most intense temperature field. Good homogeneous properties are observed in both solutions. The maximum temperature peak reaches the value of 14,085.40 K.

Figures 44 to 47 present the pressure and temperature contours calculated by the VL and LS schemes when employing the CGL collocation points. Again the LS scheme predicts the most severe pressure field, with the pressure peak being 40.0 unities more severe. Both schemes capture the two normal shock waves, ahead of the bigger ellipse and ahead of the minor ellipse. The LS scheme is less dissipative than the VL scheme. Figures 46 and 47 exhibit the temperature contours, where the most intense temperature field is due to the VL scheme, with the temperature peak reaching the value of 14,339.50 K.

Figures 48 to 51 show the pressure and the translational/rotational temperature contours generated by the VL and LS schemes as employing the LGR collocation points. The most intense pressure field is due to the LS scheme, with the pressure peak being about 55.0 unities more strength than the VL pressure peak. Good homogeneous properties are observed. Figures 50 and 51 exhibit the temperature contours generated by the VL and LS algorithms, respectively. The most intense temperature field is due to the VL scheme again, with temperature peak being about 2,500 K hotter than the LS respective field. The LS algorithm is less dissipative than the VL one. The maximum temperature peak captured by the VL scheme has the value of 14,597.90 K.

Figures 52 to 55 present the pressure and temperature contours calculated by the VL and LS schemes when using the LGL collocation points. The pressure contours generated by the LS scheme is more intense than the respective one of the VL scheme, being about 60.0 unities more strength. The most intense temperature contours are obtained by the VL scheme, with the temperature peak circa of 3,000 K hotter than the LS' temperature peak. Good homogeneous properties are observed in both figures. The two normal shock waves are captured by both schemes. The maximum temperature peak calculated by the VL scheme reaches the value of 15,228.70 K.

Viscous case. Figures 56 to 59 show the pressure and temperature contours obtained by the VL and LS schemes as employing the CGR collocation points. The pressure field generated by the VL scheme is more intense than the respective one generated by the LS scheme, with the pressure peak being 10.0 unities more strength than the latter. The most intense temperature field is obtained by the VL scheme again, reaching a maximum of

16,584.60 K at the double ellipse nose. The two normal shock waves are well captured by the both schemes. The LS scheme is less dissipative than the VL scheme.

Figures 60 to 63 exhibit the pressure and the translational/rotational temperature contours generated by the VL and LS schemes when employing the CGL collocation points. The pressure field generated by the VL algorithm is more strength than the respective one of the LS algorithm. Figures 62 and 63 show the temperature contours obtained by the VL and LS schemes, respectively. The most intense temperature field is generated by the VL scheme again, with a peak of about 17,804.90 K, circa of 1,600 K higher than the LS' temperature peak.

Figures 64 to 67 present the pressure and temperature contours calculated by the VL and LS algorithms when using the LGR collocation points. The most intense pressure field is due to LS and good homogeneous properties are observed in both solutions. The LS pressure peak is circa of 50.0 unities more intense than the VL pressure peak. Figures 66 and 67 show the temperature contours obtained by the VL and LS schemes, respectively. The most intense temperature field is generated by the VL algorithm again, reaching the maximum value of 18,468.20 K, about 800.0 K higher than the LS temperature peak. It is possible to identify the viscous shock layer close to the body surface in the VL's solution.

Figures 68 to 71 show the pressure and translational/rotational temperature contours obtained by the VL and LS schemes as employing the LGL collocation points. The LS algorithm captures the most intense pressure field, with pressure peak about 50.0 unities more strength than the VL pressure peak. Figures 70 and 71 exhibit the temperature contours calculated by the VL and LS algorithms, respectively. The most intense temperature field is due to the VL algorithm, with the temperature peak of 18,453.10 K. Effects of the viscous shock layer were well captured. The two normal shock waves are well detected by both schemes.

8.3. Quantitative Analysis

In order to perform a quantitative analysis, the present reactive results are compared to the perfect gas solutions. The stagnation temperatures at the blunt body nose and at the double ellipse nose were evaluated assuming the perfect gas formulation. Such parameter calculated at this way is not the best comparison, but in the absence of practical reactive results, it constitutes the best available solution.

To calculate the stagnation temperatures ahead of the blunt body and ahead of the double ellipse configurations, [37] presents a formula for this parameter head of the configuration as function of the normal shock wave properties. Equation (48) was picked up from this reference.

$$T_0 = T_{initial}\left(1+\frac{\gamma-1}{2}M^2_{initial}\right). \quad (48)$$

In the present study, considering the CO_2 as a perfect gas and that the Mars atmosphere is composed basically of this gas, one obtains for the theoretical stagnation temperatures the values exhibited in Tab. 4, where γ_{CO2} was obtained from [35]. Values of numerical stagnation temperatures are exhibited in Tabs. 5 (inviscid case) and 6 (viscous case). The minimum percentage error for the blunt body problem in the inviscid case was due to VL scheme using the LGL collocation point variant with a value of 0.26%, whereas for the viscous case was due to VL scheme using the CGL collocation point variant with a value of 1.29%.For the double ellipse problem, the minimum percentage error for the inviscid case was due to VL scheme using the LGL collocation point variant with a value of 3.88%, whereas for the viscous case was due to LS scheme using the CGR collocation point variant with a value of 0.77%.

As the hypersonic flow around the blunt body was simulated with a zero value to the attack angle, a zero lift coefficient is the expected value for this aerodynamic coefficient in this problem. Tables 7(inviscid case) and 8 (viscous case) exhibit an analysis of the lift aerodynamic coefficient, based only on pressure contribution, in this study. As can be observed, the best value to the lift coefficient in the inviscid case was obtained by the VL scheme when using the LGR collocation points, whereas in the viscous case was obtained by the LS scheme when using also the LGR collocation points.

8.4. Computational Performance

Tables 9 (inviscid case) and 10 (viscous case) present the computational data of the VL and LS schemes for both problems. It shows the CFL number and the number of iterations to convergence for all studied cases in the

current work. It can be verified that the best performance of the VL scheme occurred when using the LGR collocation points in the blunt body inviscid case with a CFL of 0.50, converging in 235 iterations, whereas of the LS scheme occurred when using the LGL collocation points in the blunt body inviscid case with a CFL of 0.40, converging in 252 iterations. The global analysis highlights the VL scheme using the LGR collocation points in the inviscid case as the best method in terms of convergence ratio.

As final conclusion, it is possible to highlight the LGL collocation points, in its fifth-order of accuracy, for the inviscid case, as the best performance in estimating the stagnation temperature ahead of the blunt body configuration, with an error of 0.26%, when coupled with the VL scheme, and the LGR collocation points, in its eighth-order of accuracy, for the viscous case, as the best performance is estimating the lift aerodynamic coefficient around the blunt body configuration when coupled with the LS scheme. On the other hand, in the double ellipse problem, the CGR collocation points, in its eighth-order of accuracy, for the viscous case, was the best performance in estimating the stagnation temperature, with an error of 0.77%, when coupled with the LS scheme. Moreover, the LGR collocation points, in its fifth-order of accuracy, for the inviscid case, when coupled with the VL scheme, were globally the most efficient in terms of computational effort. It is also important to note that all Legendre variants of the spectral method predicted the stagnation temperature value with errors inferior to 25.00% for the inviscid case, whereas the Chebyshev variants of the spectral method predicted the stagnation temperature value with errors inferior to 13.00% for the viscous case.

Finally, to close this work, the computational cost of the numerical schemes using the several types of collocation points is presented in Tab. 11. For the inviscid case, the cheapest combination was the LS scheme using CGL collocation points and the LGL collocation points with a cost of 0.0011401 sec/per-volume/per-iteration, whereas for the viscous case the cheapest was due to the VL scheme coupled with the LGL collocation points with a cost of 0.0011683 sec/per-volume/per-iteration.

Table 1: Values of S_x and S_y.

Surface	**S_x**	**S_y**
i,j-1/2	$\left(y_{i+1,j} - y_{i,j}\right)$	$\left(x_{i,j} - x_{i+1,j}\right)$
i+1/2,j	$\left(y_{i+1,j+1} - y_{i+1,j}\right)$	$\left(x_{i+1,j} - x_{i+1,j+1}\right)$
i,j+1/2	$\left(y_{i,j+1} - y_{i+1,j+1}\right)$	$\left(x_{i+1,j+1} - x_{i,j+1}\right)$
i-1/2,j	$\left(y_{i,j} - y_{i,j+1}\right)$	$\left(x_{i,j+1} - x_{i,j}\right)$

Table 2: Initial conditions to the blunt body problem

Property	**Value**
$M_{initial}$	31.0
$\rho_{initial}$	0.0002687 kg/m^3
$pr_{initial}$	8.3039 Pa
$U_{initial}$	6,155 m/s
$T_{initial}$	160.9 K
Altitude	41,700 m
c_N	0.00
c_O	0.00
c_{N_2}	0.03
c_{O_2}	0.00
c_{NO}	0.00
c_{CO_2}	0.97
c_C	0.00
c_{CO}	0.00

c_{CN}	0.00
L	1.7 m
Re_{char}	$3.23x10^5$

Table 3: Initial conditions to the double ellipse problem

Property	**Value**
$M_{initial}$	26.0
$\rho_{initial}$	0.000265 kg/m^3
$pr_{initial}$	8.1394 Pa
$U_{initial}$	5,210 m/s
$T_{initial}$	160.0 K
Altitude	44,000 m
c_N	0.00
c_O	0.00
c_{N_2}	0.0270
c_{O_2}	0.0015
c_{NO}	0.00
c_{CO_2}	0.9715
c_C	0.00
c_{CO}	0.00
c_{CN}	0.00
L	5.00 m
Re_{char}	$8.04x10^5$

Table 4: Theoretical value of the stagnation temperature

Physical Problem:	**γ_{CO2}:**	**$M_{initial}$:**	**$T_{initial}$:**	**T_0(Theoretical):**
Blunt body	1.29	31.0	160.9K	22,581.51K
Double ellipse	1.29	26.0	160.0K	15,843.20K

Table 5: Values of stagnation temperature and respective errors in the inviscid case (5th order of accuracy)

Problem	**Scheme:**	**Spectral Model – Collocation Points:**	**T_0 (Numerical):**	**Error (%):**
	VL[(1)]	Chabyshev-Gauss-Radau	16,522.70	26.83
	LS[(2)]	Chabyshev-Gauss-Radau	17,411.40	22.90
	VL	Chabyshev-Gauss-Lobatto	17,892.20	20.77
Blunt Body	LS	Chabyshev-Gauss-Lobatto	18,191.10	19.44
(T_0 = 22,581.51K)	VL	Legendre-Gauss-Radau	21,727.90	3.78
	LS	Legendre-Gauss-Radau	20,869.90	7.58
	VL	Legendre-Gauss-Lobatto	22,640.50	0.26
	LS	Legendre-Gauss-Lobatto	21,445.90	5.03
	VL	Chabyshev-Gauss-Radau	12,288.00	22.44
	LS	Chabyshev-Gauss-Radau	14,085.40	11.09
	VL	Chabyshev-Gauss-Lobatto	14,339.50	9.49
Double Ellipse	LS	Chabyshev-Gauss-Lobatto	12,751.90	19.51
(T_0 = 15,843.20K)	VL	Legendre-Gauss-Radau	14,597.90	7.86
	LS	Legendre-Gauss-Radau	11,925.70	24.73
	VL	Legendre-Gauss-Lobatto	15,228.70	3.88
	LS	Legendre-Gauss-Lobatto	12,320.40	22.24

(1): Van Leer; (2): Liou and Steffen Jr.

Table 6: Values of stagnation temperature and respective errors in the viscous case (8th order of accuracy)

Problem:	Scheme:	Spectral Model – Collocation Points:	T_0 (Numerical):	Error (%):
	VL	Chabyshev-Gauss-Radau	21,721.60	3.81
	LS	Chabyshev-Gauss-Radau	20,271.00	10.23
	VL	Chabyshev-Gauss-Lobatto	22,872.70	1.29
Blunt Body	LS	Chabyshev-Gauss-Lobatto	20,864.20	7.60
(T_0 = 22,581.51K)	VL	Legendre-Gauss-Radau	26,222.10	16.12
	LS	Legendre-Gauss-Radau	24,060.20	6.55
	VL	Legendre-Gauss-Lobatto	26,225.80	16.14
	LS	Legendre-Gauss-Lobatto	24,103.50	6.74
	VL	Chabyshev-Gauss-Radau	16,584.60	4.68
	LS	Chabyshev-Gauss-Radau	15,721.10	0.77
	VL	Chabyshev-Gauss-Lobatto	17,804.90	12.38
Double Ellipse	LS	Chabyshev-Gauss-Lobatto	16,334.70	3.10
(T_0 = 15,843.20K)	VL	Legendre-Gauss-Radau	18,408.20	16.19
	LS	Legendre-Gauss-Radau	17,620.60	11.22
	VL	Legendre-Gauss-Lobatto	18,453.10	16.47
	LS	Legendre-Gauss-Lobatto	17,602.90	11.11

Table 7: Lift aerodynamic coefficient in the blunt body inviscid case (5th order of accuracy)

Scheme:	Spectral Model – Collocation Points:	c_L:
VL	Chabyshev-Gauss-Radau	$-2.5912\text{x}10^{-14}$
LS	Chabyshev-Gauss-Radau	$9.1525\text{x}10^{-15}$
VL	Chabyshev-Gauss-Lobatto	$-3.9787\text{x}10^{-14}$
LS	Chabyshev-Gauss-Lobatto	$-5.1117\text{x}10^{-14}$
VL	Legendre-Gauss-Radau	$-3.5279\text{x}10^{-15}$
LS	Legendre-Gauss-Radau	$-3.5730\text{x}10^{-15}$
VL	Legendre-Gauss-Lobatto	$7.3782\text{x}10^{-15}$
LS	Legendre-Gauss-Lobatto	$-1.8605\text{x}10^{-14}$

Table 8: Lift aerodynamic coefficient in the blunt body viscous case (8th order of accuracy).

Scheme:	Spectral Model – Collocation Points:	c_L:
VL	Chabyshev-Gauss-Radau	$6.0827\text{x}10^{-15}$
LS	Chabyshev-Gauss-Radau	$-3.7306\text{x}10^{-14}$
VL	Chabyshev-Gauss-Lobatto	$1.3908\text{x}10^{-14}$
LS	Chabyshev-Gauss-Lobatto	$-2.3846\text{x}10^{-15}$
VL	Legendre-Gauss-Radau	$-1.0009\text{x}10^{-14}$
LS	Legendre-Gauss-Radau	$-1.3129\text{x}10^{-16}$
VL	Legendre-Gauss-Lobatto	$2.7935\text{x}10^{-15}$
LS	Legendre-Gauss-Lobatto	$4.7036\text{x}10^{-16}$

Table 9: Computational data for the inviscid case

March Method:	Scheme:	Spectral Model – Collocation Points:	CFL:	Iterations:
	VL	Chabyshev-Gauss-Radau	0.70	427
	LS	Chabyshev-Gauss-Radau	0.70	681
	VL	Chabyshev-Gauss-Lobatto	0.70	410
Blunt Body	LS	Chabyshev-Gauss-Lobatto	0.70	564
	VL	Legendre-Gauss-Radau	0.50	235
	LS	Legendre-Gauss-Radau	0.50	564
	VL	Legendre-Gauss-Lobatto	0.10	1,414

	LS	Legendre-Gauss-Lobatto	0.50	309
	VL	Chabyshev-Gauss-Radau	0.20	1,164
	LS	Chabyshev-Gauss-Radau	0.10	2,526
	VL	Chabyshev-Gauss-Lobatto	0.10	1,652
Double Ellipse	LS	Chabyshev-Gauss-Lobatto	0.20	949
	VL	Legendre-Gauss-Radau	0.10	872
	LS	Legendre-Gauss-Radau	0.40	281
	VL	Legendre-Gauss-Lobatto	0.10	744
	LS	Legendre-Gauss-Lobatto	0.40	252

Table 10: Computational data for the viscous case

March Method:	Scheme:	Spectral Model – Collocation Points:	CFL:	Iterations:
	VL	Chabyshev-Gauss-Radau	0.20	1,531
	LS	Chabyshev-Gauss-Radau	0.70	422
	VL	Chabyshev-Gauss-Lobatto	0.20	1,301
Blunt Body	LS	Chabyshev-Gauss-Lobatto	0.70	369
	VL	Legendre-Gauss-Radau	0.10	1,295
	LS	Legendre-Gauss-Radau	0.50	300
	VL	Legendre-Gauss-Lobatto	0.10	1,325
	LS	Legendre-Gauss-Lobatto	0.50	306
	VL	Chabyshev-Gauss-Radau	0.20	2,334
	LS	Chabyshev-Gauss-Radau	0.30	1,868
	VL	Chabyshev-Gauss-Lobatto	0.10	3,867
Double Ellipse	LS	Chabyshev-Gauss-Lobatto	0.30	1,580
	VL	Legendre-Gauss-Radau	0.10	2,131
	LS	Legendre-Gauss-Radau	0.30	906
	VL	Legendre-Gauss-Lobatto	0.10	2,116
	LS	Legendre-Gauss-Lobatto	0.30	926

Table 11: Computational cost of spectral variants

Order of Accuracy:	Scheme:	Spectral Method:	Computational Cost (seconds/volumes/iterations):
	VL	Chebyshev-Gauss-Radau	0.0016944
	LS	Chebyshev-Gauss-Radau	0.0015458
	VL	Chebyshev-Gauss-Lobatto	0.0011446
5^{th} Order	LS	Chebyshev-Gauss-Lobatto	0.0011401
(Inviscid case)	VL	Legendre-Gauss-Radau	0.0011799
	LS	Legendre-Gauss-Radau	0.0012340
	VL	Legendre-Gauss-Lobatto	0.0013220
	LS	Legendre-Gauss-Lobatto	0.0011401
	VL	Chebyshev-Gauss-Radau	0.0013224
	LS	Chebyshev-Gauss-Radau	0.0011992
	VL	Chebyshev-Gauss-Lobatto	0.0011768
8^{th} Order	LS	Chebyshev-Gauss-Lobatto	0.0012229
(Viscous case)	VL	Legendre-Gauss-Radau	0.0011758
	LS	Legendre-Gauss-Radau	0.0013643
	VL	Legendre-Gauss-Lobatto	0.0011683
	LS	Legendre-Gauss-Lobatto	0.0011832

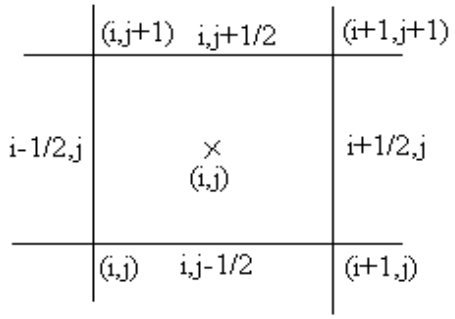

Figure 1: Computational cell

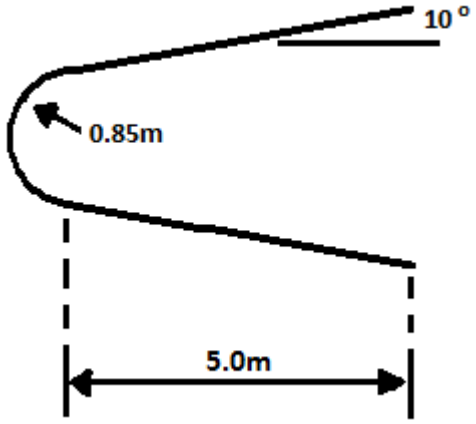

Figure 2: Blunt body geometry

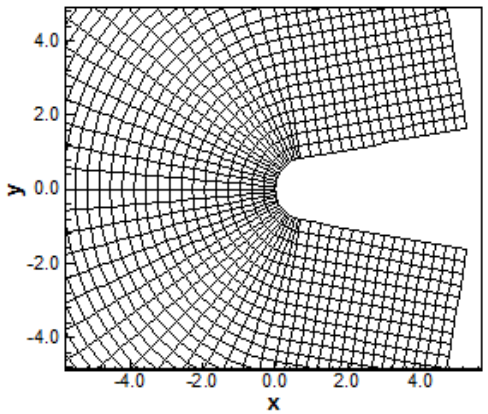

Figure 3: Blunt body mesh for inviscid flow

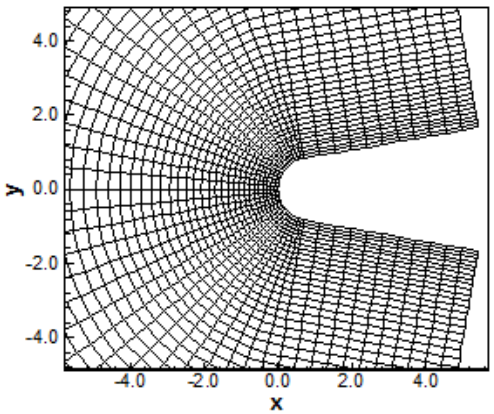

Figure 4: Blunt body mesh for viscous flow

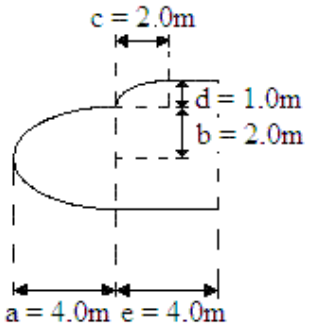

Figure 5: Double ellipse geometry

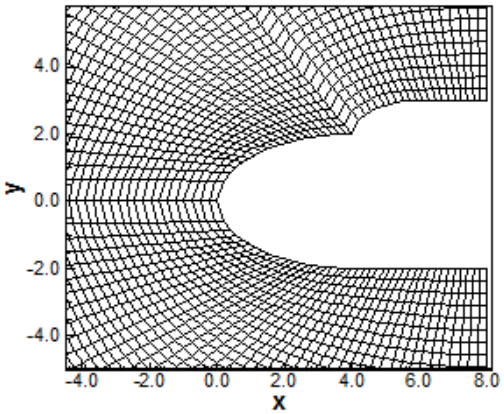

Figure 6: Double ellipse mesh for inviscid flow

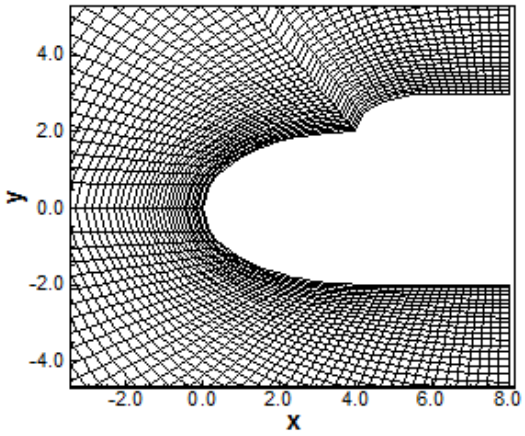

Figure 7: Double ellipse mesh for viscous flow

Inviscid Solutions – 5th Order – Blunt Body Problem

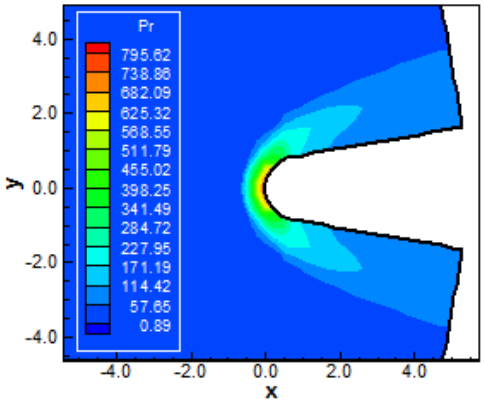

Figure 8: Pressure contours (CGR-VL)

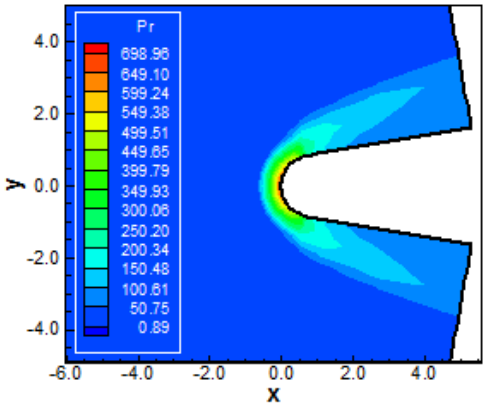

Figure 9: Pressure contours (CGR-LS)

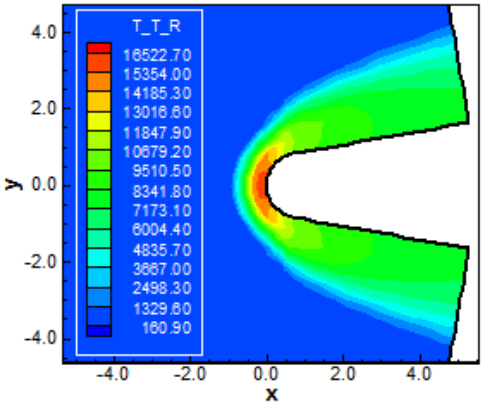

Figure 10: Translational/rotational temperature contours (CGR-VL)

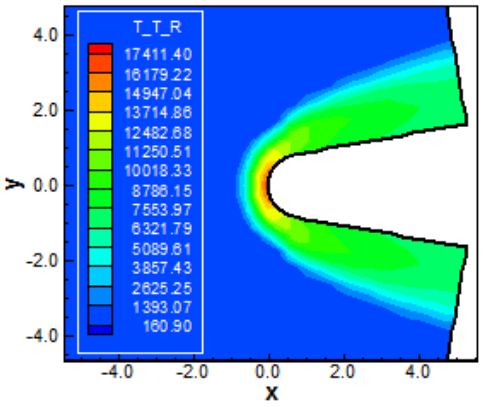

Figure 11: Translational/rotational temperature contours (CGR-LS)

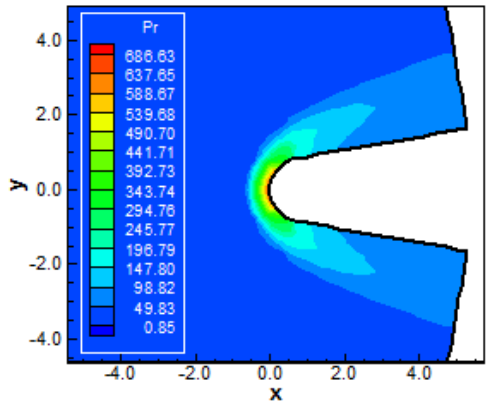

Figure 12: Pressure contours (CGL-VL)

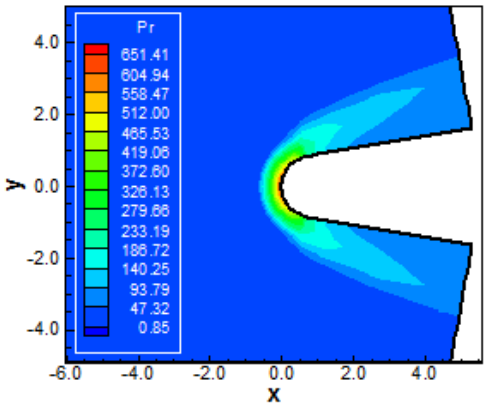

Figure 13. Pressure contours (CGL-LS)

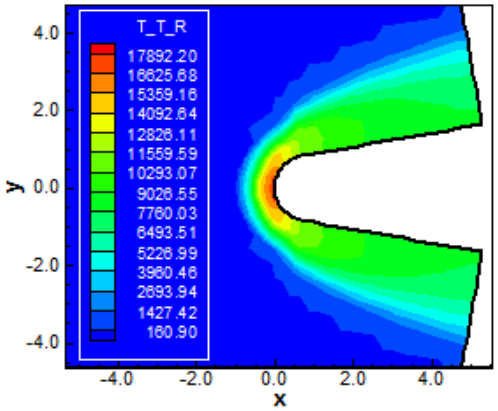

Figure 14: Translational/rotational temperature contours (CGL-VL)

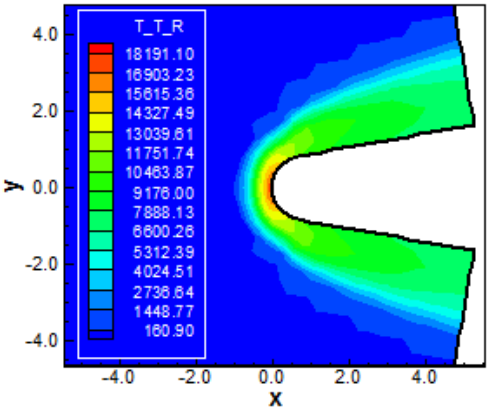

Figure 15: Translational/rotational temperature contours (CGL-LS)

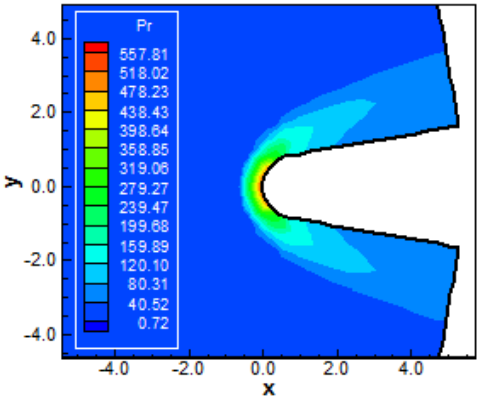

Figure 16: Pressure contours (LGR-VL)

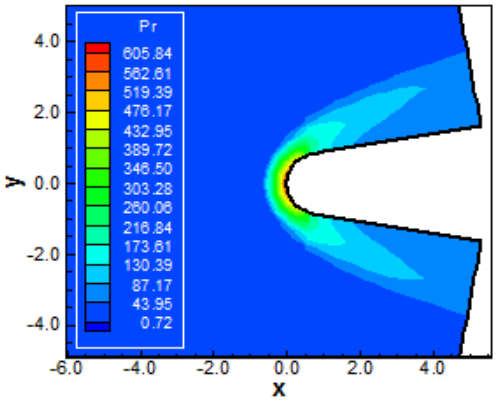

Figure 17: Pressure contours (LGR-LS)

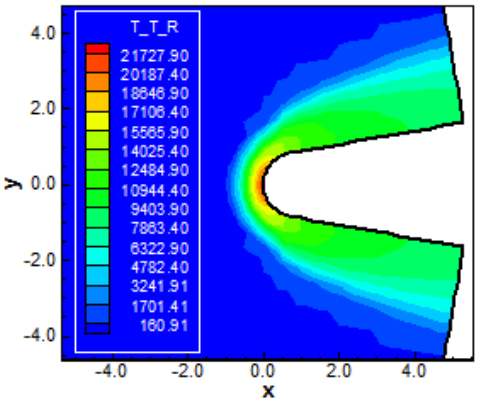

Figure 18: Translational/rotational temperature contours (LGR-VL)

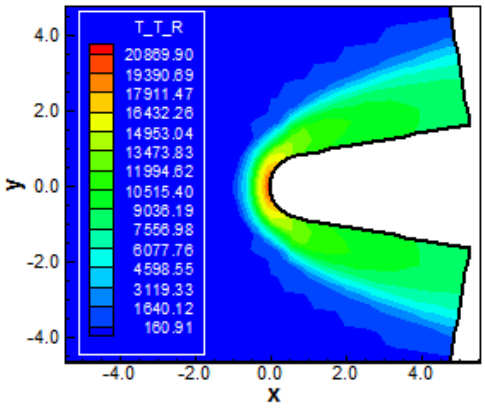

Figure 19: Translational/rotational temperature contours (LGR-LS)

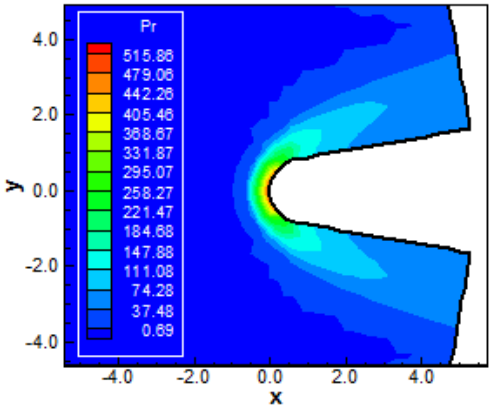

Figure 20: Pressure contours (LGL-VL)

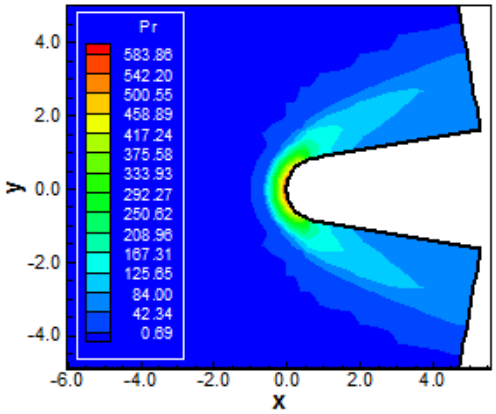

Figure 21: Pressure contours (LGL-LS)

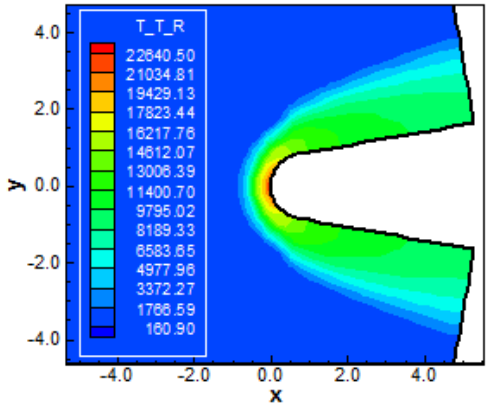

Figure 22: Translational/rotational temperature contours (LGL-VL)

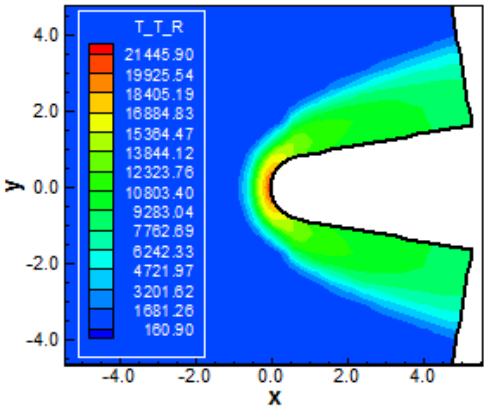

Figure 23: Translational/rotational temperature contours (LGL-LS)

Viscous Solutions – 8th Order – Blunt Body Problem

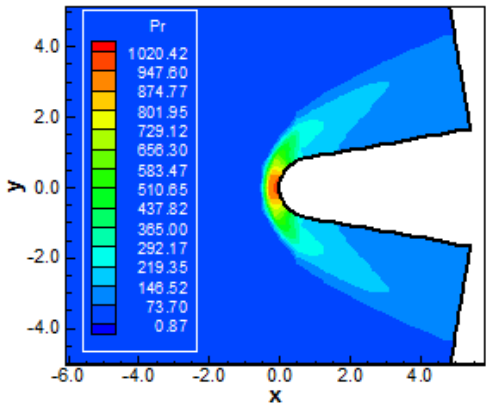

Figure 24: Pressure contours (CGR-VL)

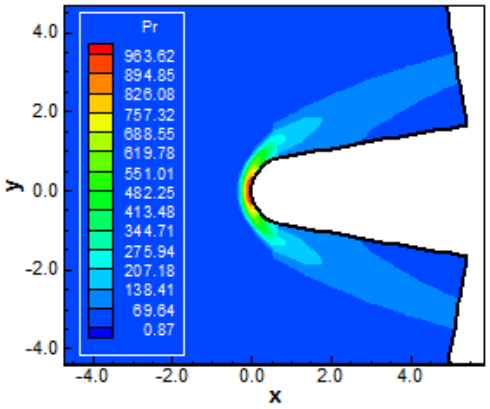

Figure 25: Pressure contours (CGR-LS)

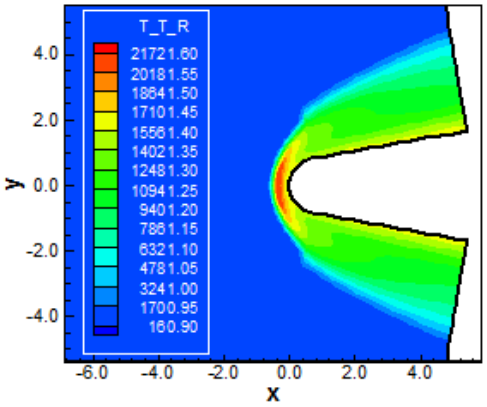

Figure 26: Translational/rotational temperature contours (CGR-VL)

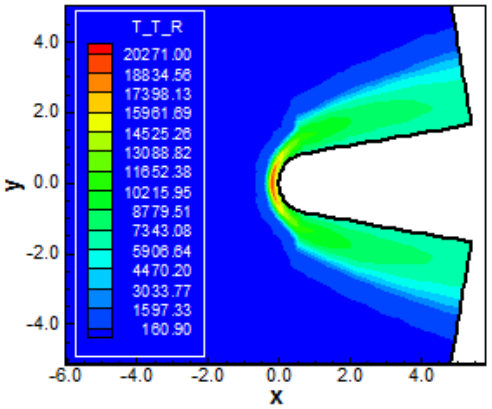

Figure 27: Translational/rotational temperature contours (CGR-LS)

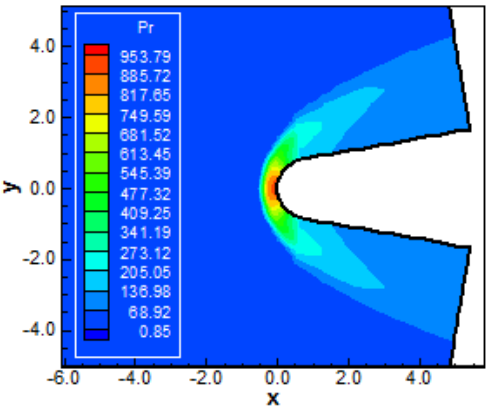

Figure 28: Pressure contours (CGL-VL)

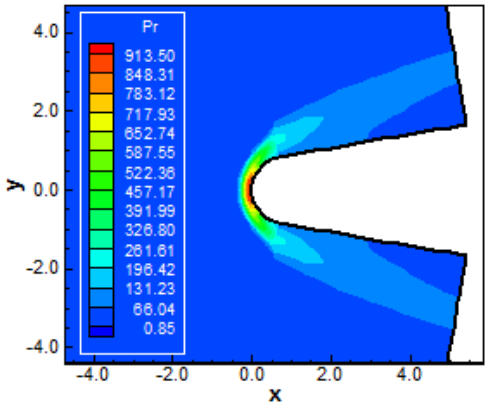

Figure 29: Pressure contours (CGL-LS)

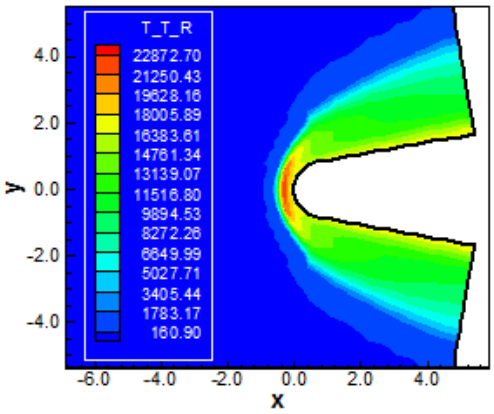

Figure 30: Translational/rotational temperature contours (CGL-VL)

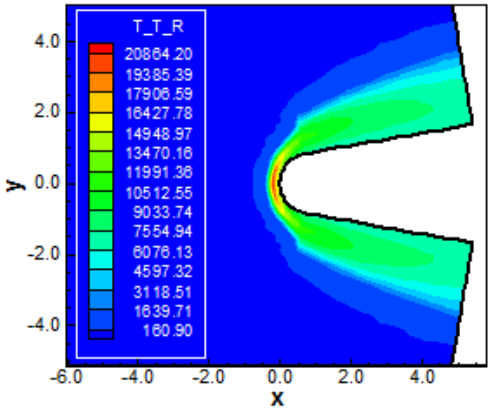

Figure 31: Translational/rotational temperature contours (CGL-LS)

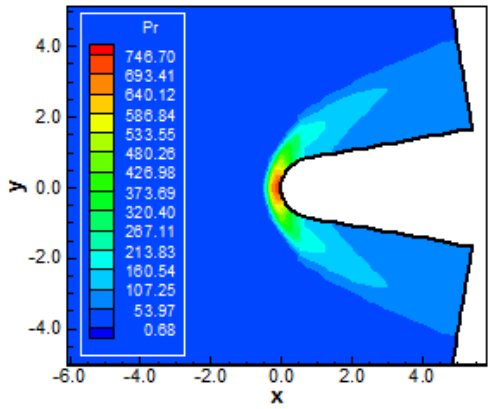

Figure 32: Pressure contours (LGR-VL)

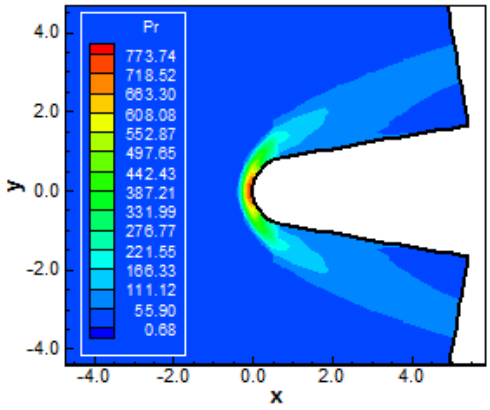

Figure 33: Pressure contours (LGR-LS)

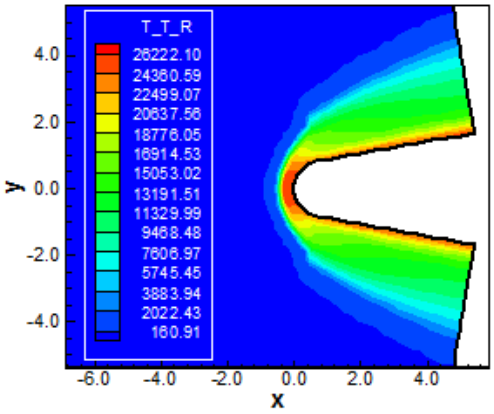

Figure 34: Translational/rotational temperature contours (LGR-VL)

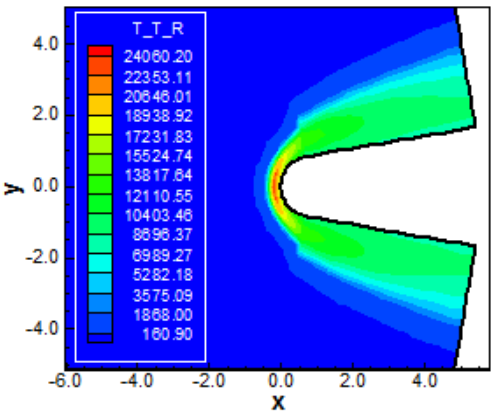

Figure 35: Translational/rotational temperature contours (LGR-LS)

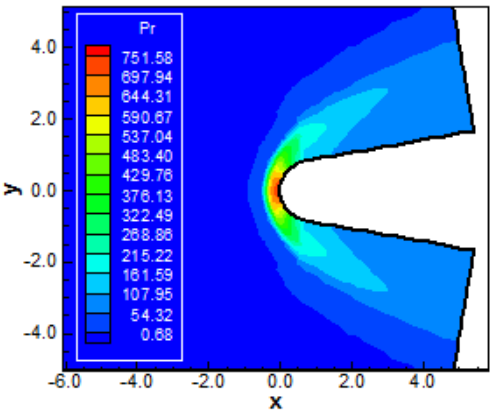

Figure 36: Pressure contours (LGL-VL)

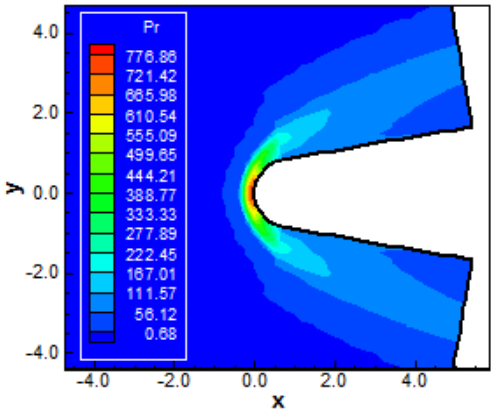

Figure 37: Pressure contours (LGL-LS)

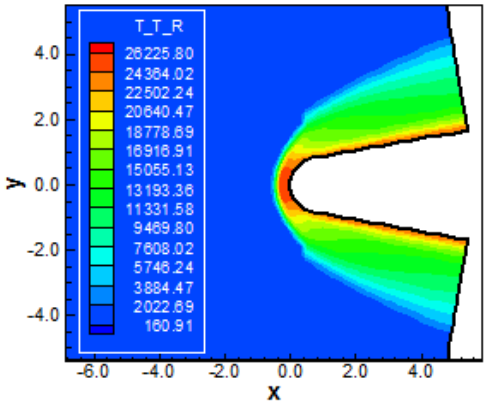

Figure 38: Translational/rotational temperature contours (LGL-VL)

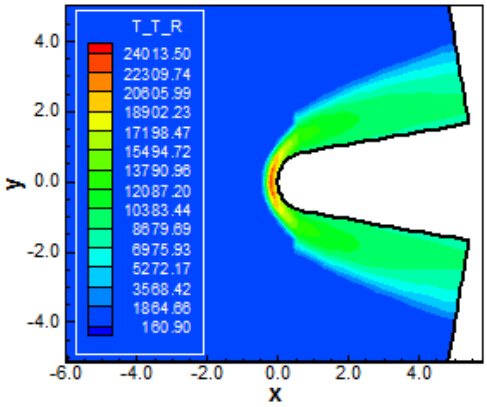

Figure 39: Translational/rotational temperature contours (LGL-LS)

Inviscid Solutions – 5th Order – Double Ellipse Problem

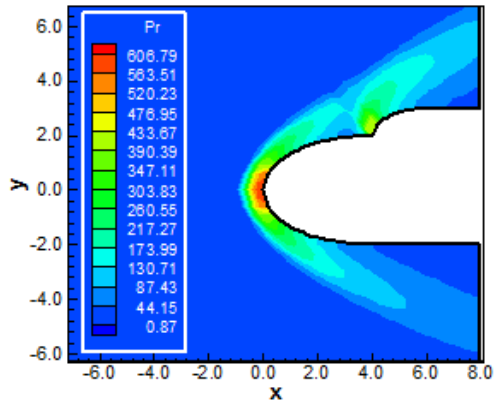

Figure 40: Pressure contours (CGR-VL)

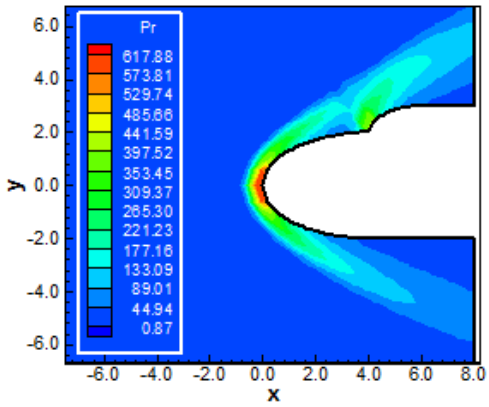

Figure 41: Pressure contours (CGR-LS)

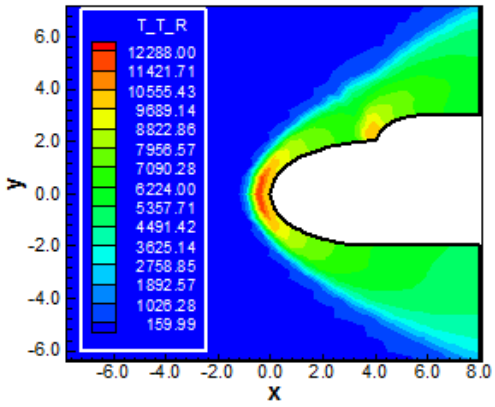

Figure 42: Translational/rotational temperature contours (CGR-VL)

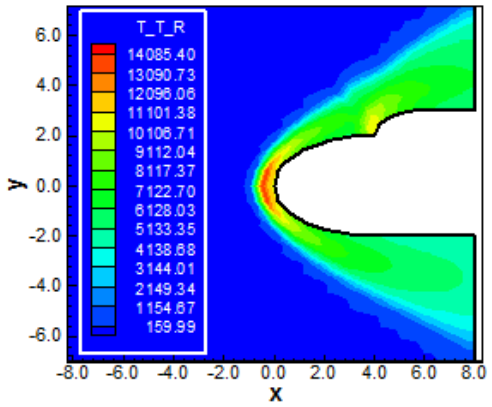

Figure 43: Translational/rotational temperature contours (CGR-LS)

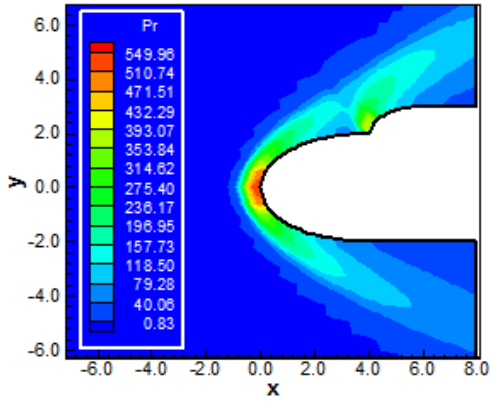

Figure 44: Pressure contours (CGL-VL)

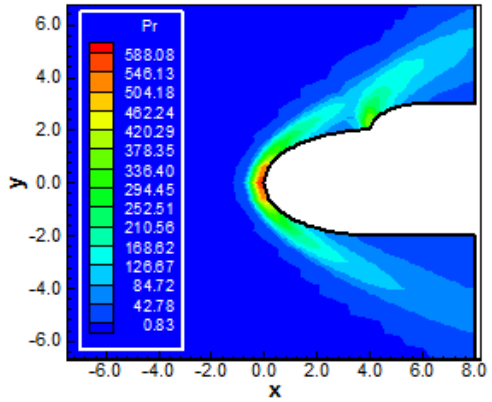

Figure 45: Pressure contours (CGL-LS)

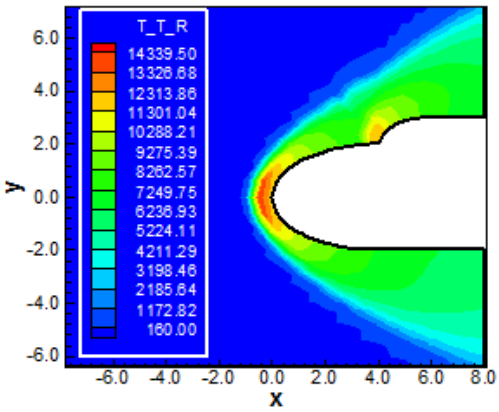

Figure 46: Translational/rotational temperature contours (CGL-VL)

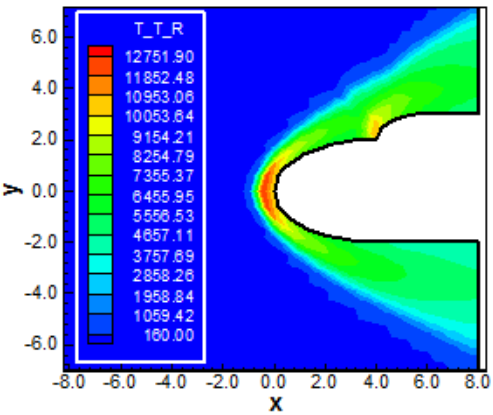

Figure 47: Translational/rotational temperature contours (CGL-LS)

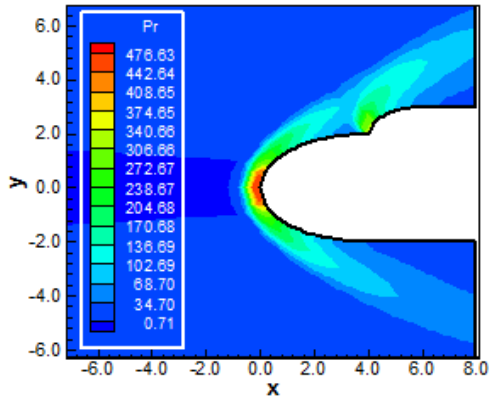

Figure 48: Pressure contours (LGR-VL)

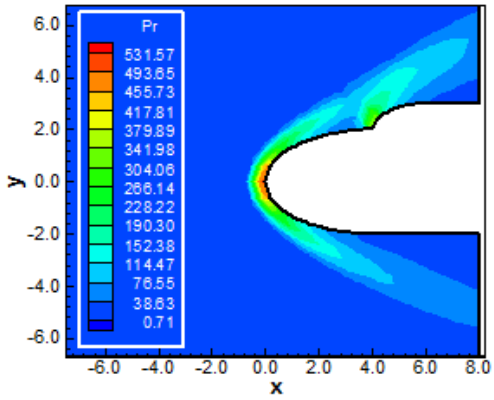

Figure 49: Pressure contours (LGR-LS)

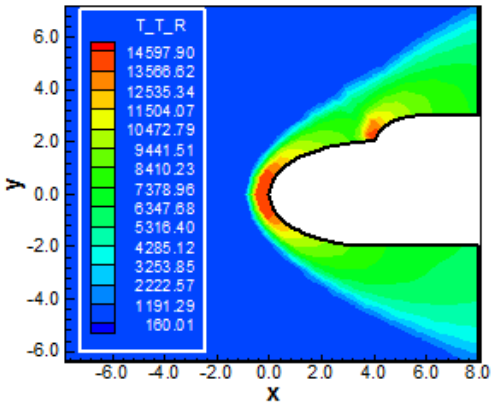

Figure 50: Translational/rotational temperature contours (LGR-VL)

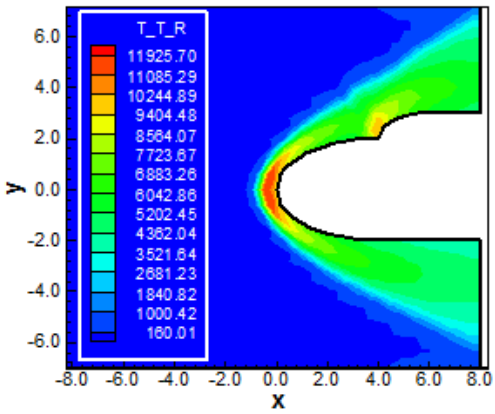

Figure 51: Translational/rotational temperature contours (LGR-LS)

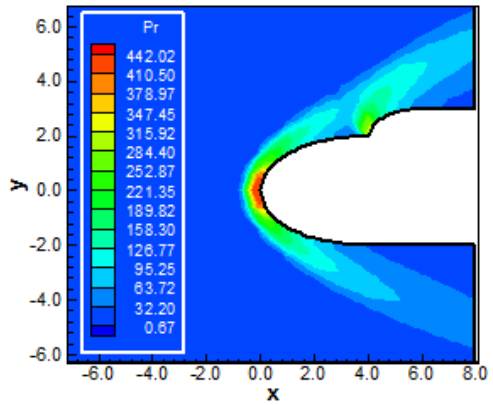

Figure 52: Pressure contours (LGL-VL)

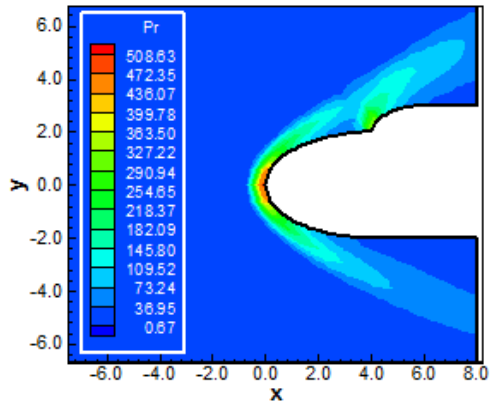

Figure 53: Pressure contours (LGL-LS)

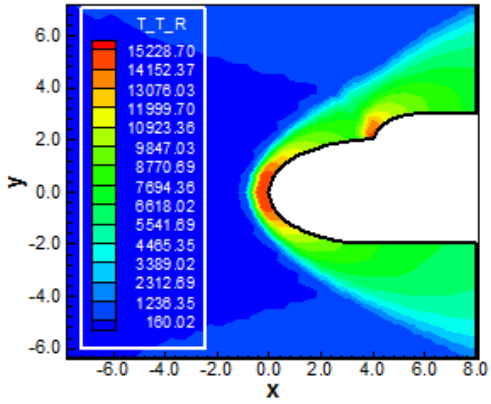

Figure 54: Translational/rotational temperature contours (LGL-VL)

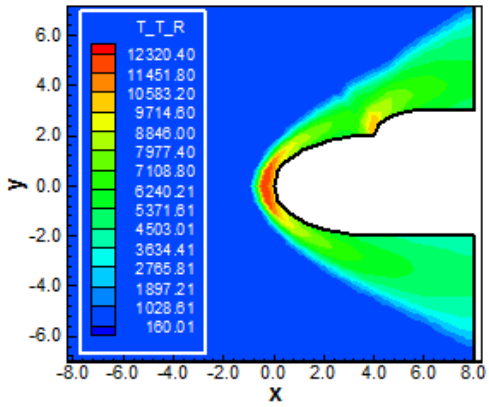

Figure 55: Translational/rotational temperature contours (LGL-LS)

Viscous Solutions – 8th Order – Double Ellipse Problem

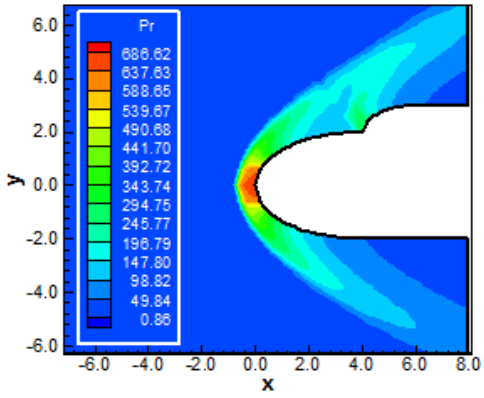

Figure 56: Pressure contours (CGR-VL)

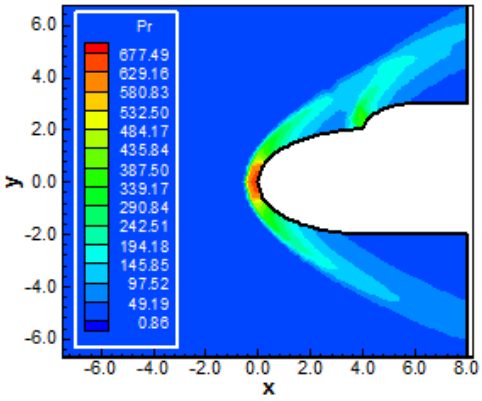

Figure 57: Pressure contours (CGR-LS)

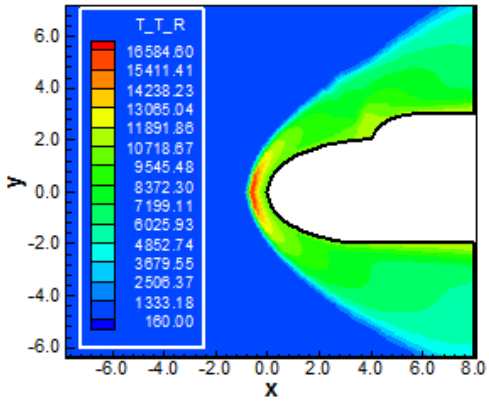

Figure 58: Translational/rotational temperature contours (CGR-VL)

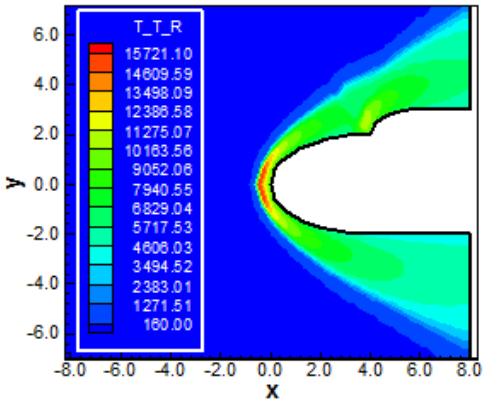

Figure 59: Translational/rotational temperature contours (CGR-LS)

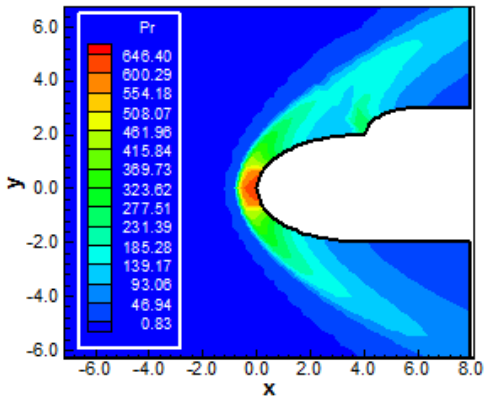

Figure 60: Pressure contours (CGL-VL)

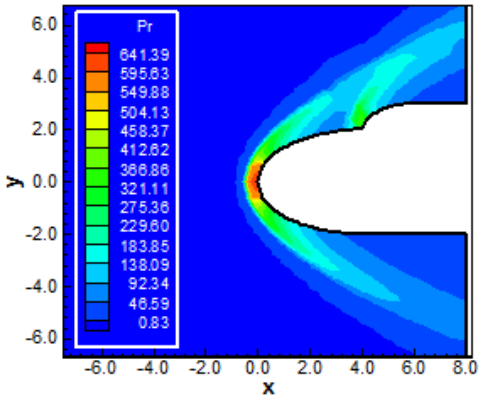

Figure 61: Pressure contours (CGL-LS)

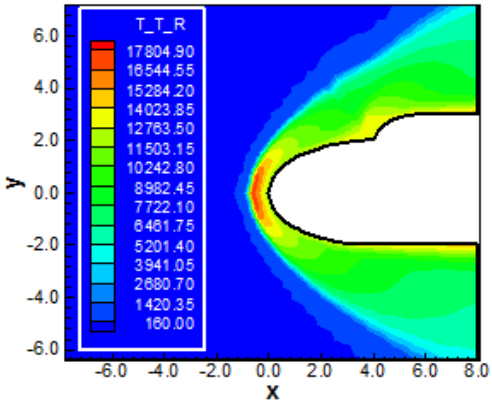

Figure 62: Translational/rotational temperature contours (CGL-VL)

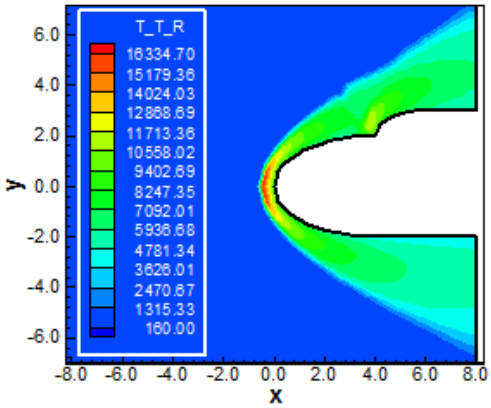

Figure 63: Translational/rotational temperature contours (CGL-LS)

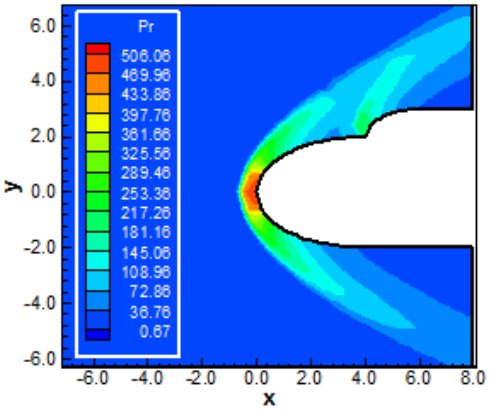

Figure 64: Pressure contours (LGR-VL)

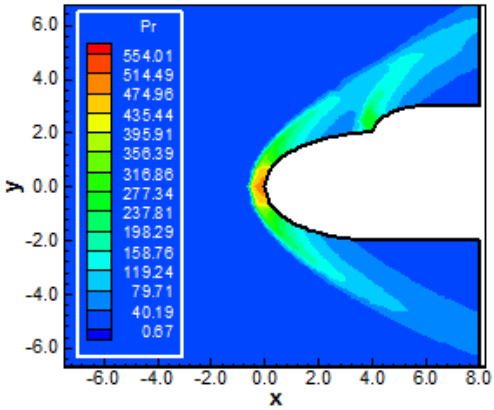

Figure 65: Pressure contours (LGR-LS)

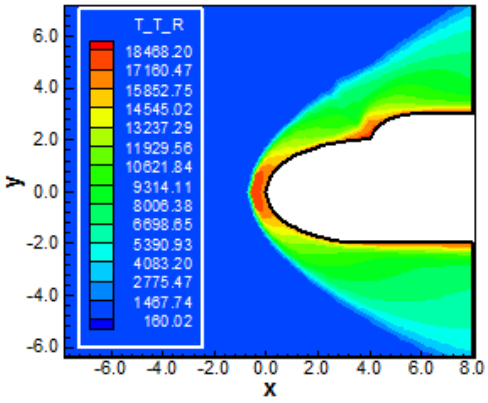

Figure 66: Translational/rotational temperature contours (LGR-VL)

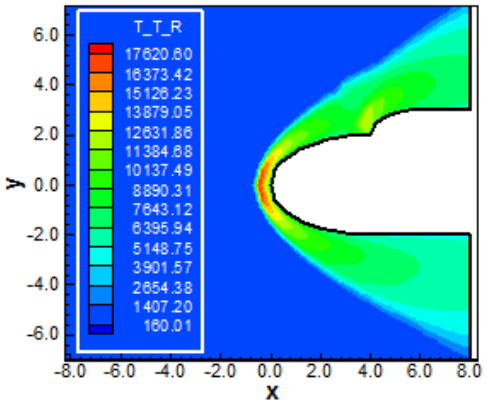

Figure 67: Translational/rotational temperature contours (LGR-LS)

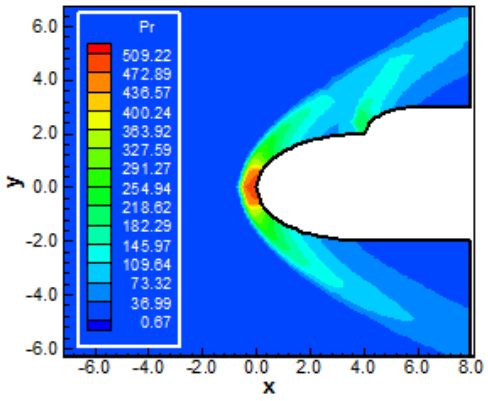

Figure 68: Pressure contours (LGL-VL)

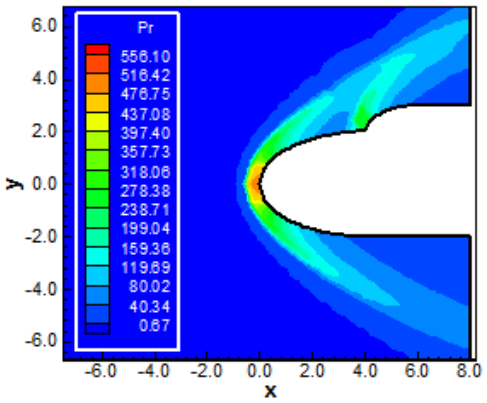

Figure 69: Pressure contours (LGL-LS)

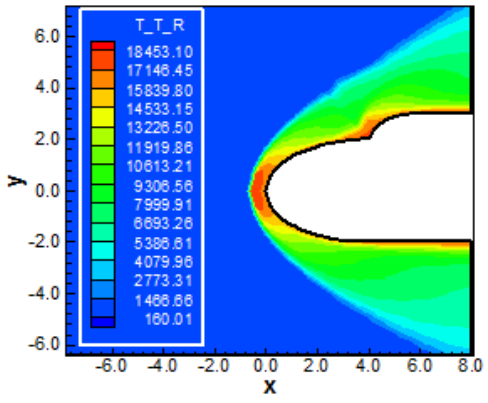

Figure 70: Translational/rotational temperature contours (LGL-VL)

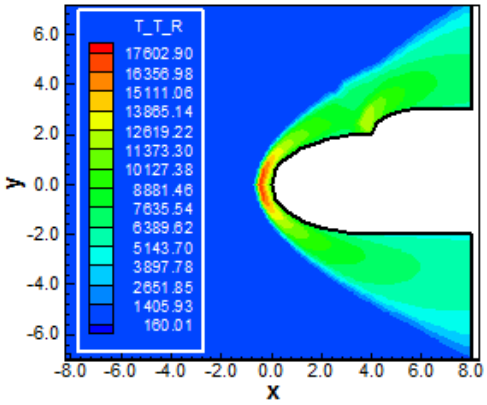

Figure 71. Translational/rotational temperature contours (LGL-LS)

9. Conclusions

In the present work, a study involving a spectral method to solve the reactive Euler and Navier-Stokes equations under condition of entry flow in Mars was performed. The Euler and Navier-Stokes equations, in conservative and finite volume contexts, employing structured spatial discretization, were studied. The [17-18] schemes were used to perform the numerical experiments. The Euler backward integration method was applied to march the schemes in time. The spectral method presented in this work employed collocation points and variants of

Chebyshev and Legendre interpolation functions were analyzed. The "hot gas" hypersonic flows around a blunt body, and around a double ellipse in two-dimensions, were simulated. The convergence process was accelerated to steady state condition through a spatially variable time step procedure, which has proved effective gains in terms of computational acceleration [19-20]. The reactive simulations involved Mars atmosphere chemical model of nine species and fifty-three reactions, based on the [21] model. N, O, N_2, O_2, NO, CO_2, C, CO, CN species were used to perform the numerical comparisons. The results have indicated that all Legendre variants of the spectral method predicted the stagnation temperature value with errors inferior to 25.00% for the inviscid case, whereas the Chebyshev variants of the spectral method predicted the stagnation temperature value with errors inferior to 13.00% for the viscous case.

As final conclusion, it is possible to highlight the Legendre-Gauss-Lobatto collocation points, in its fifth-order of accuracy, for the inviscid case, as the best performance in estimating the stagnation temperature ahead of the blunt body configuration, with an error of 0.26%, when coupled with the [17] scheme, and the Legendre-Gauss-Radau collocation points, in its eighth-order of accuracy, for the viscous case, as the best performance is estimating the lift aerodynamic coefficient around the blunt body configuration when coupled with the [18] scheme. On the other hand, in the double ellipse problem, the Chebyshev-Gauss-Radau collocation points, in its eighth-order of accuracy, for the viscous case, was the best performance in estimating the stagnation temperature, with an error of 0.77%, when coupled with the [18] scheme. Moreover, the Legendre-Gauss-Radau collocation points, in its fifth-order of accuracy, for the inviscid case, when coupled with the [17] scheme, were globally the most efficient in terms of computational effort. It is also important to note that all Legendre variants of the spectral method predicted the stagnation temperature value with errors inferior to 25.00% for the inviscid case, whereas the Chebyshev variants of the spectral method predicted the stagnation temperature value with errors inferior to 13.00% for the viscous case.

Finally, to close this work, the computational cost of the numerical schemes using the several types of collocation points was presented in Tab. 11. For the inviscid case, the cheapest combination was the [18] scheme using Chebyshev-Gauss-Lobatto collocation points and the Legendre-Gauss-Lobatto collocation points with a cost of 0.0011401 sec/per-volume/per-iteration, whereas for the viscous case the cheapest was due to the [17] scheme coupled with the Legendre-Gauss-Lobatto collocation points with a cost of 0.0011683 sec/per-volume/per-iteration.

10. Motivation and Novelty

The motivation to study spectral methods applied to reentry flow was enormous because of some papers in the CFD literature report for such methods as the state of art of high order resolution. The intention of this paper was to propose a different spectral method that was of easy implementation and conformed about author's ideas of treating the governing equations of fluid flow. The formulation presented here is for a thermochemical non-equilibrium condition and a two-temperature model. Two physical problems were also a challenge that we accepted to lead with. The results with good accuracy represent a motivation to extend the present formulation to more species and different chemical conditions.

The novelty of the present study was to implement such different spectral method to treat thermochemical non-equilibrium reentry flows and to formulate the appropriate equations for accepting this method. The robustness and convergence features of this spectral method are very impressive. While the author had to use CFL numbers of order 0.10 for his MUSCL second-order explicit method, CFL numbers as great as 0.70 for his explicit spectral method were of common use. The proposed spectral method is different from the standard spectral ones on a sense that in the latter, the differential equations and the solution method are discretized with spectral tools, whereas in the former, only the vector of conserved variables and the convective fluxes should be discretized according to the spectral tools. The result is a robust and fast solver to treat the fluid-dynamic of reentry flows.

11. Future Works

For the future, the author should extend the present formulation for an eleven species chemical model under the condition of thermochemical non-equilibrium in two-dimensions. After that, they should extend to the desired three-dimensional studies. Moreover, its implementation with turbulence effects and magnetic field actuation,

that the author consider as the state of the art project, is an objective to be reached, in both, two- and three-dimensions. Finally, the interpretation of the present formulation to two-dimensional unstructured studies is also a goal to be reached.

Acknowledgments
The author would like to thank the ITA facilities that allowed the realization of this work. He would also like to thank the CAPES by the financial support conceded under the form of a scholarship.

References

[1]. Barnes CJ, Huang GP, Shang JS. A high resolution spectral method for the compressible Navier-Stokes equations. AIAA Paper 2011-0049; 2011.
[2]. Huang P, Wang ZJ, Liu Y. An implicit space-time spectral difference method for discontinuity capturing using adaptive polynomials. AIAA Paper 2005-5255; 2005.
[3]. Huang P. High order discontinuity capturing using adaptive polynomials. AIAA paper 2006-0305; 2006.
[4]. Steger JL, Warming RF. Flux vector splitting of the inviscid gas dynamic equations with application to finite difference methods. Journal of Computational Physics, 1981; 40: 263-293.
[5]. Hughes T. The finite element method, linear static and dynamic finite element analysis. Prentice-Hall, Inc.
[6]. Lele S. Compact finite difference schemes with spectral-like resolution. Journal of Computational Physics, 1991; 103: 16-42.
[7]. Gottlieb D, Orszag S. Numerical analysis of spectral methods: theory and applications. Society for Industrial and Applied Mathematics, Philadelphia.
[8]. Hussaini MY, Kopriva DA, Salas MD, Zang TA. Spectral methods for the Euler equations: Part I – Fourier methods and shock capturing. AIAA Journal, 1985; 23(1): 64-70.
[9]. Slater JC. Electronic energy bands in metal. Physical Review, 1934; 45: 794-801.
[10]. BartaJ. Ü ber die naherungsweise l ü sung einigerzweidimensionalerelastizit ä tsaufgaben. Zeitschriftfuer Angewandte Mathematik und Mechanik, 1937; 17: 184-185.
[11]. Frazer RA, Jones WP, Skan SW. Approximation to functions and to the solutions of differential equations. Aeronautical Research Council, London. R & M 1799; 1937.
[12]. Lanczos CL. Trigonometric interpolation of empirical and analytic functions. Journal of Mathematics and Physics, 1938; 17: 123-199.
[13]. Gottlieb D, Lustman L, Orszag SA. Spectral calculations of one-dimensional inviscid compressible flows. SIAM Journal of Scientific and Statistical Computation, 1981; 2: 296-310.
[14]. Taylor TD, Meyers RB, Albert JH. Pseudospectral calculations of shock waves, rarefaction waves and contact surfaces. Computers and Fluids, 1981; 9: 469-473.
[15]. Zang TA, Hussaini MY. Mixed spectral-finite difference approximations for slightly viscous flows. Proceedings of the 7th International Conference on Numerical Methods in Fluid Dynamics. Edited by W. C. Reynolds and R. W. MacCormack. Lecture Notes in Physics, Springer-Verlag, New York, 1981;(141): 461-466.
[16]. ESA, MARSNET – Assessment study report.ESA Publication SCI, 1991; 91(6).
[17]. Van LeerB. Flux-vector splitting for the Euler equations. Lecture Notes in Physics, Springer Verlag, Berlin, 1982; 170: 507-512.
[18]. LiouM, Steffen Jr.CJ. A new flux splitting scheme. Journal of Computational Physics, 1993; 107: 23-39.
[19]. Maciel ESG. Simulations in 2D and 3D applying unstructured algorithms, Euler and Navier-Stokes equations – Perfect gas formulation. Saarbrücken, Deutschland: Lambert Academic Publishing (LAP). 2015; Ch. 1: 26-47.

[20]. Maciel ESG. Simulations in 2D and 3D applying unstructured algorithms, Euler and Navier-Stokes equations – Perfect gas formulation. Saarbrücken, Deutschland: Lambert Academic Publishing (LAP).2015; Ch. 6: 160-181.
[21]. Kay RD, Netterfield MP. Thermochemical non-equilibrium computations for a Mars entry vehicle. AIAA Paper 93-2841; 1993.
[22]. Hussaini MY, Streett CL, Zang TA. Spectral methods for partial differential equations. ICASE Report No. 83-46; 1983.
[23]. Davis PA, Rabinowitz P. Numerical Integration. Blaisdell Publishing Co.; 1967.
[24]. Canuto C, Hussaini MY, Quarteroni A, Zang TA. Spectral methods evolution to complex geometries and applications to fluid dynamics. Scientific Computation Springer, 2007.
[25]. Maciel ESG. Hypersonic reactive flow simulations in two- and three-dimensions, chemical and thermochemical non-equilibrium conditions. Saarbrücken, Deutschland: Lambert Academic Publishing (LAP). 2015; Ch. 1: 15-94.
[26]. Maciel ESG. Hypersonic reactive flow simulations in two- and three-dimensions, chemical and thermochemical non-equilibrium conditions. Saarbrücken, Deutschland: Lambert Academic Publishing (LAP). 2015; Ch. 2:95-160.
[27]. Prabhu RK. An implementation of a chemical and thermal nonequilibrium flow solver on unstructured meshes and application to blunt bodies. NASA CR-194967; 1994.
[28]. Saxena SK, Nair MT. An improved Roe scheme for real gas flow. AIAA Paper 2005-0587; 2005.
[29]. Maciel ESG, Pimenta AP. Thermochemical non-equilibrium entry flows in Mars in two-dimensions – Part I. WSEAS Transactions on Applied and Theoretical Mechanics, 2013; 8(1): 26-54.
[30]. Maciel ESG, Pimenta AP. Thermochemical non-equilibrium entry flows in Mars in two-dimensions – Part II. WSEAS Transactions on Mathematics, 2014; 13(2): 201-223.
[31]. Ait-Ali-Yahia D, Habashi WG. Finite element adaptive method for hypersonic thermochemical nonequilibrium flows. AIAA Journal, 1997; 35(8): 1294-1302.
[32]. Radespiel R, Kroll N. Accurate flux vector splitting for shocks and shear layers.Journal of Computational Physics, 1995; 121: 66-78.
[33]. Long LN, Khan MMS, Sharp HT. Massively parallel three-dimensional Euler / Navier-Stokes method. AIAA Journal, 1991; 29(5): 657-666.
[34]. Vincent WG, Kruger Jr.CH. Introduction to physical gas dynamics. Malabar, Florida, EUA: Krieger Publishing Company. 2002; Ch. 1: 1-26.
[35]. Fox RW, McDonald AT. Introdução à mecânica dos fluidos. Guanabara Editor, 1988.
[36]. Maciel ESG. Simulação numérica de escoamentos supersônicos e hipersônicos utilizando técnicas de dinâmica dos fluidos computacional. Doctoralthesis, ITA, CTA, São José dos Campos, SP, Brazil; 2002.
[37]. Anderson Jr. JD. Fundamentals of aerodynamics. McGraw-Hill, Inc., 5th Edition, 1008p.; 2010.